Surface-state bands on silicon as electron systems in reduced dimensions at atomic scales

REVIEW ARTICLE

Surface-state bands on silicon as electron systems in reduced dimensions at atomic scales

Shuji Hasegawa

Department of Physics, Graduate School of Science, University of Tokyo, 7-3-1 Hongo, Bunkyo-ku, Tokyo 113-0033, Japan
and
Core Research for Evolutional Science and Technology, The Japan Science and Technology Corporation, Kawaguchi Centre Building, Hon-cho 4-1-8, Kawaguchi, Saitama 332-0012, Japan

Abstract.   When foreign atoms to a depth of around one atomic layer adsorb on silicon crystal surfaces, the adsorbates rearrange themselves by involving the substrate Si atoms; this results in peculiar periodic atomic arrangements, *surface superstructures*, in just the topmost surface layers. Then, characteristic electronic states are created there, which are sometimes quite different from the bulk electronic states in the interior of the crystal, leading to novel properties only at the surfaces. Here, surface superstructures are introduced that have two-dimensional or quasi-one-dimensional metallic electronic states on silicon surfaces. Sophisticated surface science techniques, e.g., scanning tunnelling microscopy, photoemission spectroscopy, electron-energy-loss spectroscopy, and microscopic four-point probes reveal characteristic phenomena such as phase transitions accompanying symmetry breakdown, electron standing waves, charge-density waves, sheet plasmons, and surface electronic transport, in which surface-state bands play main roles. These results show that surface superstructures on silicon provide fruitful platforms on which to investigate the physics of atomic-scale low-dimensional electron systems.

1. Introduction

A silicon crystal has a diamond lattice, in which each Si atom has four 'hands' (valence electrons) with which to make covalent bonds with four neighbours in a tetrahedral arrangement. But, imagine the atoms in the topmost layer on the crystal surface. They do not have neighbours on one side, so they will have unpaired electrons, or *dangling bonds*. Since a high density of dangling bonds will make the surface unstable, the surface atoms spontaneously rearrange themselves to reduce the number of dangling bonds. As a result, peculiar, but regular atomic arrangements occur in one or two atomic layers on surfaces to stabilize the surfaces. The resulting atomic arrangements are called *surface superstructures*; this is a kind of self-organization phenomenon. On clean surfaces without any foreign adsorbates, clean surface superstructures are created. When some foreign atoms adsorb on the surfaces, they are arranged involving the substrate Si atoms to attain more energetically favourable structures, *adsorbate-induced surface superstructures*. Already, almost all of the kinds of atom in the periodic table have been deposited on silicon surfaces with different coverages and substrate temperatures, and more than 300 kinds of surface superstructure found [1]. Different adsorbates and different atomic arrangements naturally form different surface electronic states. Since the surface superstructures are formed only in one or two surface atomic layers, their surface-state bands are inherently two-dimensional, which should be contrasted with the case for

conventional two-dimensional electron gas (2DEG) systems in bulk electronic states formed at semiconductor heterojunctions or surface inversion layers with pronounced band bendings. Sometimes, one-dimensional electronic bands are created due to strongly anisotropic atom arrangements in surface superstructures. A large number of previous studies have revealed the characteristic atomic and electronic structures of surface superstructures, which are never expected in the bulk crystals. Surfaces with such a variety of structures are frequently called *surface phases of materials*.

As the next step of research, some people have begun to study physical properties characteristic of such surface superstructures; electrical, magnetic, and optical properties inherent in the surface states are now active targets in surface science. In this review article, I describe some manifestations of the low-dimensional nature of surface-state electrons, such as electron standing waves, sheet plasmons in a two-dimensional (2D) metallic state, and Peierls transition in a quasi-one-dimensional (1D) metallic surface state. Next I introduce some experimental methods of detection of electrical conduction through surface-state bands using the phenomenon of carrier doping into the surface-state bands and a newly developed technique using microscopic four-point probes. These will display characteristic phenomena only at surfaces and provide unique experimental verifications just for surfaces.

2. Surface-state bands

Let me introduce surface-state bands using the schematic illustration in figure 1. When the valence electrons $(3s)^2(3p)^2$ of a Si atom form hybrid orbitals sp^3 to make bonds with neighbouring atoms, their energy levels split into bonding and anti-bonding states. The valence electrons are accommodated in the bonding state, so the anti-bonding state is empty.
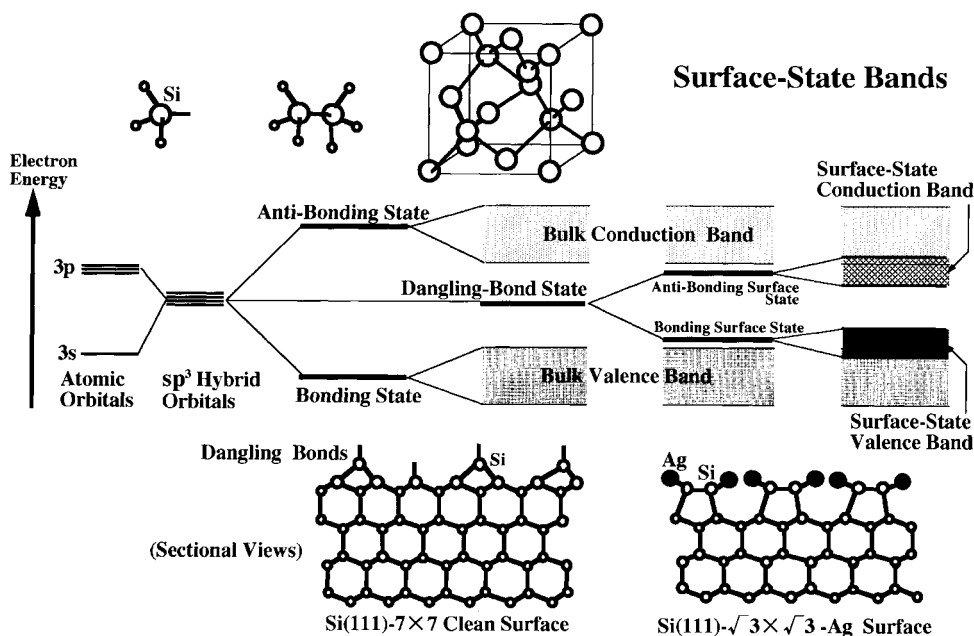

Figure 1. A schematic energy diagram for atoms and molecules, and also the bulk and the surface of a silicon crystal.

Since in a crystal many atoms make bonds with each other to arrange themselves periodically, these energy levels are broadened to make bands: the valence band and the conduction band, respectively. These are electronic states in a bulk crystal. But on the surface, as mentioned before, there exist dangling bonds (unpaired hybrid orbitals), which are similar to the hybrid orbitals of isolated atoms, whose energy levels will be located between the bonding and anti-bonding states, or within an energy gap. In fact, the dangling-bond state on a clean Si(111) surface is known to lie around the middle of the band gap [2, 3]. But when foreign atoms come to make bonds with the topmost Si atoms, the dangling-bond state will again split into bonding and anti-bonding states. When, furthermore, the adsorbates induce a surface superstructure to form some orbital overlaps between neighbouring sites, the bonding and anti-bonding states will again be broadened and become bands. These are *surface-state bands*, inherent in the surface superstructure. The bands have their own characters, independent of the bulk electronic states.

3. Two-dimensional metal; the Si(111)–$\sqrt{3} \times \sqrt{3}$-Ag surface

3.1. Atomic structure

Let me give the first example, the Si(111)–$\sqrt{3} \times \sqrt{3}$-Ag surface superstructure (figure 2(a)), which is formed by depositing one monolayer (ML) of Ag atoms on a Si(111) surface at temperatures higher than 250 °C. 'One ML' means that the atom density is equal to that of the topmost layer of the Si(111) face, 7.8×10^{14} atoms cm^{-2}. This surface superstructure has been a long-standing target in surface science because of the interesting physics revealed in its atomic arrangement, surface electronic states, and electronic transport phenomena [4–6]. After a long period of controversy, over 20 years, its atomic arrangement has been solved by the so-called *honeycomb-chained-triangle (HCT)* model [7, 8], in which each Ag atom makes an ionic–covalent bond with a substrate Si atom, leaving no dangling bonds, resulting in an exceptionally stable surface. Figure 2(a) illustrates the HCT model, believed to be the most stable atomic arrangement for the $\sqrt{3} \times \sqrt{3}$-Ag superstructure (at least) at room temperature (RT). The Ag atoms do not make metallic bonds with each other. The Si atoms in the topmost layer arrange in an unusual way by making trimers, while the underlying Si layers form a conventional tetrahedral diamond lattice. In this way, only the two layers on the surface have a peculiar, but regular structure, of which the unit cell, $\sqrt{3} \times \sqrt{3}$ times the fundamental bulk unit cell, is indicated in figure 2(a). There are two Ag triangles in the unit cell, which are connected to each other to make a honeycomb-lattice pattern, so this structure is called the HCT structure; it was first proposed by Takahashi *et al* [7] on the basis of surface x-ray diffraction investigations, with confirmations following from other experimental and theoretical works. This model explains well the scanning tunnelling micrographs (STM) [9, 10], and empty-state (figure 2(b)) and filled-state images (figure 2(c)) at RT. Protrusions in the empty-state image, corresponding to the centres of the Ag triangles, are arranged in a honeycomb-lattice pattern in figure 2(b). This surface is now regarded as a prototypical metal-covered semiconductor system, used as a kind of standard example for, e.g., high-resolution photoemission spectroscopy (PES) [11], atomic-force microscopy [12–14], x-ray diffraction for buried-interface structure analysis [15,16], studying Schottky barrier formation [17], optical second-harmonic generation spectroscopy [18], light-emission spectroscopy using STM [19], studying sheet plasmons in a surface-state band [20], and first-principles theory [9, 10, 21–23], and also used as a unique substrate for growth of C_{60} molecular layers [24–27], adatom gas phases [28], and other surface superstructures by additional metal depositions [29–36] and hydrogen adsorptions [37].
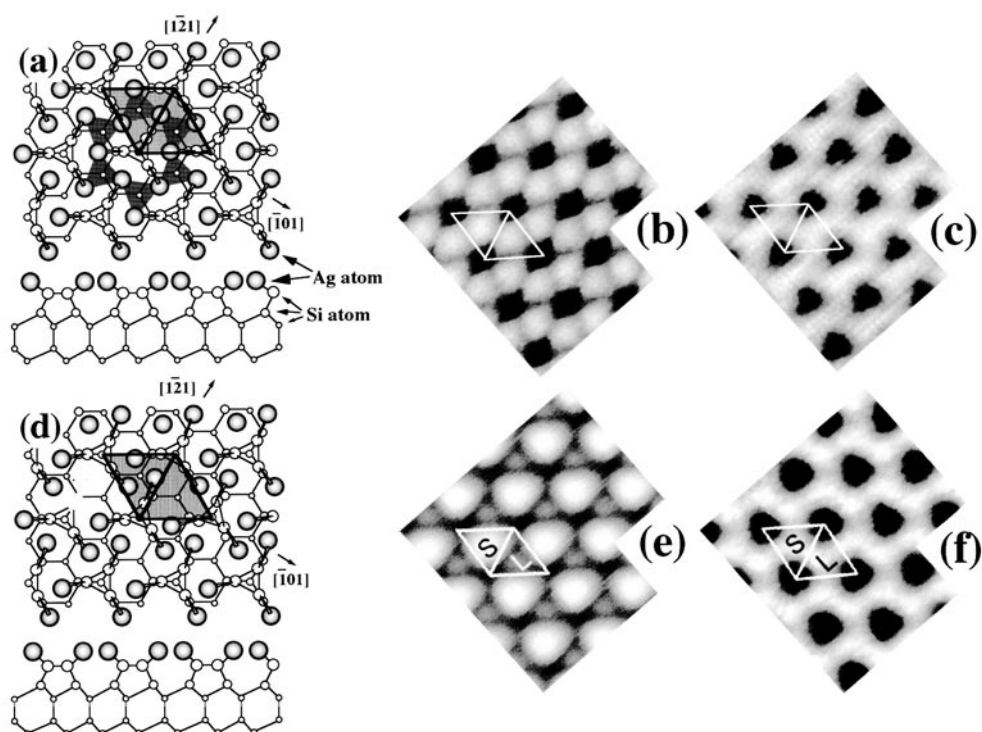
Figure 2. ((a), (d)) Schematic illustrations of atomic arrangements (upper panel: plan view; lower panel: sectional view), and ((b), (c), (e), (f)) STM images of the Si(111)–$\sqrt{3} \times \sqrt{3}$-Ag surface superstructure. (a) Its excited-state structure (the so-called honeycomb-chained-triangle (HCT) structure). Filled circles are Ag atoms, and open circles are Si ones. A $\sqrt{3} \times \sqrt{3}$ unit cell is shown. (b) Its empty-state and (c) filled-state STM images at RT. (d) Its ground-state structure (the so-called inequivalent-triangle (IET) structure). (e) Its empty-state and (f) filled-state STM images at 62 K.

However, it has recently turned out that the HCT structure is not a ground-state structure; a symmetry-broken phase, the so-called *inequivalent-triangle (IET)* structure, is more energetically favourable than the HCT structure [21, 38]. At lower temperatures (62 K), its empty-state STM image (figure 2(e)) shows different features—a hexagonal-lattice pattern, instead of the honeycomb one at RT—although the filled-state image in figure 2(f) is the same as that in figure 2(c) at RT [38]. This has turned out to correspond to a new model for the surface, the IET model, in which the Ag triangles, all of which are equivalent in the HCT model, differ in size alternately. As shown in the schematic diagram of the atomic arrangement (figure 2(d)) for the IET model, a Ag triangle in a half-unit cell becomes larger (called the L-half) and another triangle in the other half-unit cell becomes smaller (the S-half). In other words, a mirror plane along the [$1\bar{2}1$] direction in the HCT model (belonging to the $p31m$ space group) is not present in the IET model (belonging to the $p3$ space group); this is a kind of symmetry breakdown. The protrusions in the low-temperature STM image in figure 2(e) correspond to the S-half unit cell. A first-principles calculation shows that the IET structure is more stable than the HCT one by 0.1 eV per $\sqrt{3} \times \sqrt{3}$ unit cell [21].

Then we are faced with new interesting questions about this surface. What is the relation between the HCT and IET structures? There should be a phase transition between them induced by temperature changes. What is the nature of the phase transition? Moreover, it is not certain

whether the HCT structure can be understood as a time-averaged outcome of a fluctuating IET structure, much like symmetric dimers in STM images on the clean Si(001) surface at RT, which is a time-averaged buckled dimer. This surface is still a challenging target in surface physics.

3.2. Electronic structure

This superstructure has a characteristic electronic state as clarified by angle-resolved photo-emission spectroscopy (ARPES) [39–41]. On irradiating the surface with ultraviolet light, photoelectrons are emitted from the surface, whose energy and angular distributions are analysed to obtain the initial surface electronic states, i.e., the binding energy as a function of wavevector (band dispersion relation). Figure 3 shows such ARPES spectra taken from the $\sqrt{3} \times \sqrt{3}$-Ag surface at different detection angles, in which three peaks indicated by S_1, S_2, and S_3 are noticed, which are known to be surface states. These peaks change their positions with the detection angles, indicating some characteristic dispersions. From these spectra, the 2D band dispersion diagram is constructed, as shown in figure 4(a). An interesting feature here is the S_1 band, a parabolic band crossing the Fermi level (E_F). Since this band is known to be isotropic, this surface state is a *2D free-electron-like state*. Since the bottom of the band is below E_F by about 0.2 eV, some electrons (approximately 1.6×10^{13} electrons cm^{-2}) are accumulated in this surface-state band. This band is well reproduced by first-principles calculation [21], as shown in figure 4(c). The surface state S_1 is composed of a bonding state among Ag 5p orbitals in the Ag triangles, and the S_2 and S_3 states stem mainly from Ag 5s orbitals [23]. Since the S_1 state is confined to the topmost Ag layer, this provides a unique platform on which to investigate low-dimensional physics such as electronic transport, because its 'thickness' can be as small as one atomic layer—much thinner than conventional 2DEG systems formed at surface inversion layers or heterojunctions—and also because, as described below, the electron concentration in this band can be controlled by use of additional adsorbates on top of the surface

Such a 2D free-electron-like electronic state is manifested in low-temperature STM images in the form of so-called *electron standing waves* or *energy-resolved Friedel oscillations* [42]. Before going into the detail of the observations, the operating principles of the STM should be briefly described. The STM is a microscope enabling direct observations of atomic corrugation on surfaces to be carried out, by scanning a sharp metal tip laterally over the sample surface without contact. The distance between the tip and the sample surface is maintained at around 1 nm. When a voltage of around 1 V is applied at the gap, a tunnelling current I_t flows between the tip and sample, which can be approximately expressed as

$$I_t(x, y; V) \propto f(x, y; V) \exp\{-d(x, y)/\kappa\} \tag{1}$$

where the coordinates (x, y) are on the sample surface. This tells us that as the tip–sample distance $d(x, y)$ becomes smaller, a larger tunnelling current flows due to the exponential factor, and also that I_t is proportional to the tip–sample joint density of states (DOS) $f(x, y; V)$ at the position (x, y). Since the decay length κ is around 0.1 nm for most materials, the tunnelling current drops by nearly an order of magnitude for every 0.1 nm separation between the tip and sample, so one can trace the roughness of the surface with height resolution at subatomic levels by measuring the current variations while the tip is scanning laterally over the surface.

Another point that equation (1) indicates concerns the joint DOS $f(x, y; V)$. When the tip is regarded as a mathematical point source of current (the s-wave approximation), or the tip is assumed to have a constant DOS as is frequently done, $f(x, y; V)$ is simply regarded as the local DOS $\rho(x, y; E_F)$ at E_F for the sample surface with a very small bias voltage. With
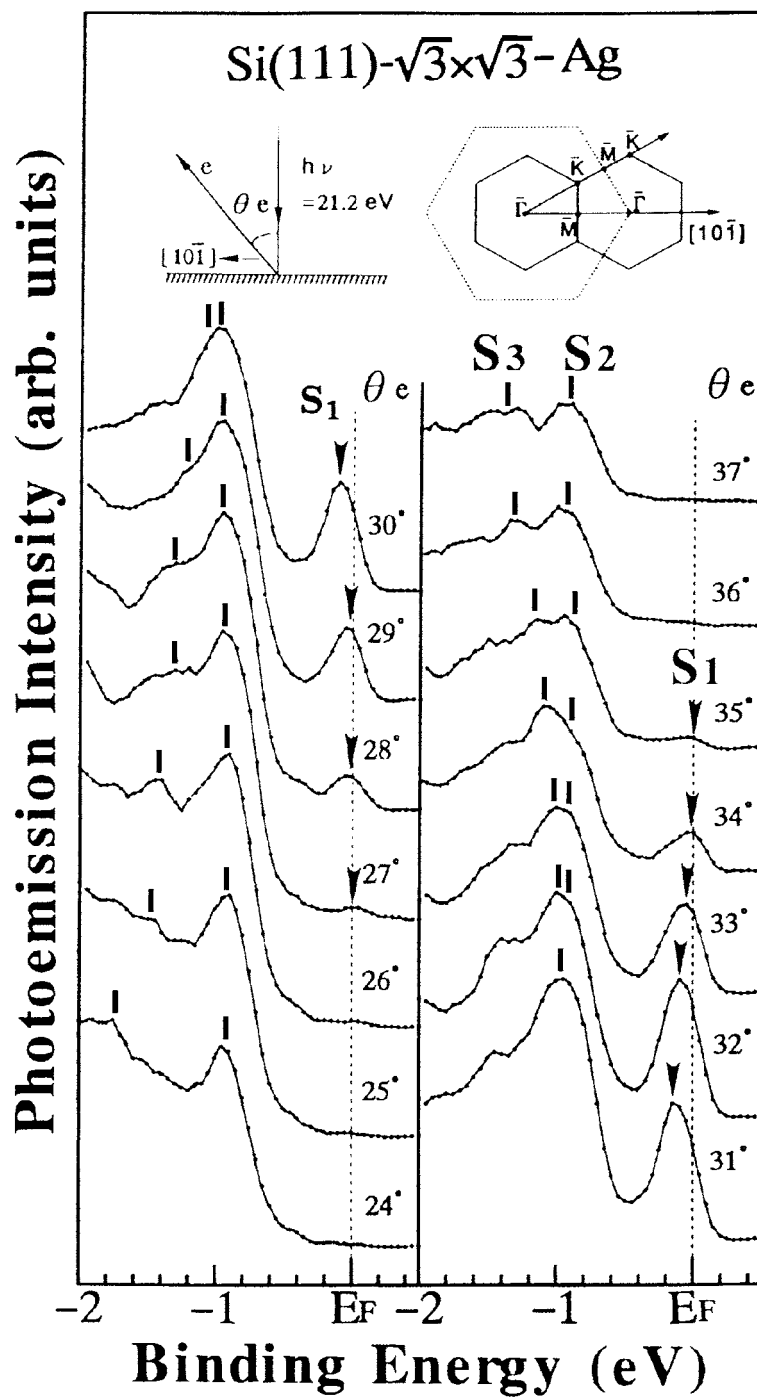
Figure 3. A series of angle-resolved photoemission spectra taken from the Si(111)–$\sqrt{3} \times \sqrt{3}$-Ag surface at RT along the [10$\bar{1}$] direction [41]. θ_e is the electron detection angle with respect to the surface normal. The unpolarized 21.2 eV light from a He lamp irradiated the sample with normal incidence.
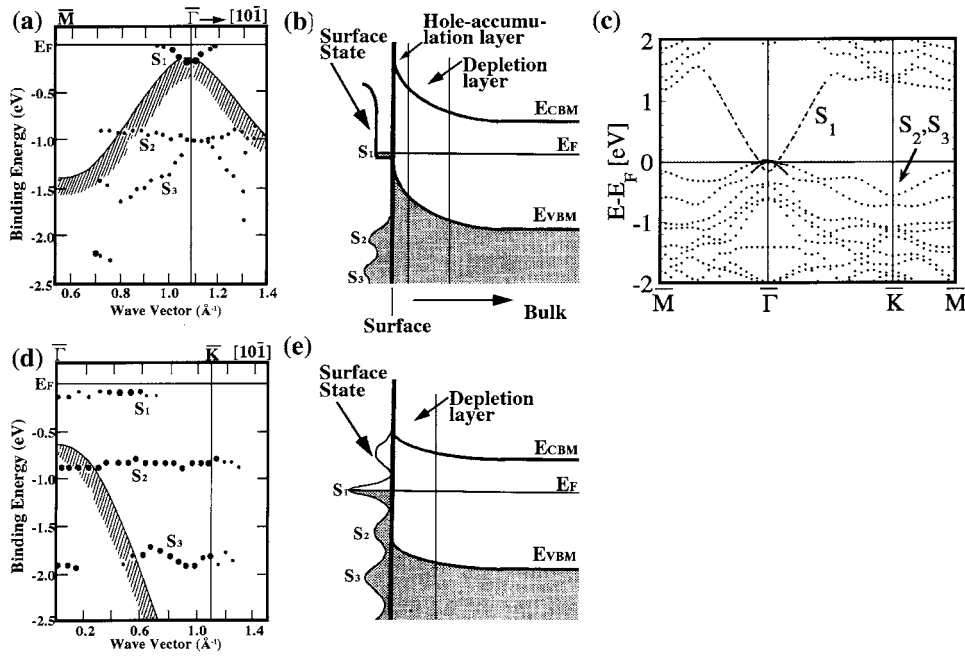
Figure 4. Electronic structures of ((a), (b), (c)) the Si(111)–$\sqrt{3} \times \sqrt{3}$-Ag surface and ((d), (e)) the Si(111)–7 × 7 clean surface. (a) and (d) show 2D band dispersion diagrams of surface states, determined by ARPES [40, 41]. $\overline{\Gamma}$ and $\overline{K}$ in (d), and $\overline{\Gamma}$ and $\overline{M}$ in (a) are symmetric points in the 1 × 1 and $\sqrt{3} \times \sqrt{3}$ surface Brillouin zones, respectively. The projected band structures of the bulk states are also included as curves with hatching. (c) The 2D band dispersion diagram obtained by first-principles calculations [21]. (b) and (e) are schematic band diagrams showing surface states and surface-space-charge layers. E_{VBM}: valence-band maximum; E_{CBM}: conduction-band minimum; E_F: Fermi level.

larger bias voltages (but much smaller than the average work function of the tip and sample, divided by e), it can be written as [43]

$$f(x, y; V) = \int_{E_F}^{E_F + eV} \rho(x, y; E) T(E, V) \, dE \qquad (2)$$

where $T(E, V)$ is the barrier transmission coefficient, which describes the probability of tunnelling of an electron at an energy level E under an applied bias voltage V. The spatial variation of the tunnelling current during the tip scanning thus reflects the local DOS of the sample surface, mixed with information on the surface topography described above. Therefore, for a surface on which the probed electronic states are localized at the surface atoms, as in the case of dangling-bond surface states on the Si(111)–7 × 7 clean surface, the protrusions observed in STM images directly correspond to the individual surface atoms. But when the probed surface electronic states have an extended wavefunction, atomic resolution will not be achieved. In general, STM images probing a surface state described by a 2D Bloch wavefunction directly show the squares of the absolute values of the cell function. The plane-wave part of the Bloch wavefunction will play a role in making the STM images take the form of electron standing waves, as described below for the Si(111)–$\sqrt{3} \times \sqrt{3}$-Ag surface.

Figure 5 shows an STM image of the $\sqrt{3} \times \sqrt{3}$-Ag surface taken at 6 K (though the 7 × 7 clean domains partially remain, because of the Ag coverage being smaller than 1 ML). In the $\sqrt{3} \times \sqrt{3}$-Ag domains, fine periodic corrugations are seen, corresponding to the $\sqrt{3} \times \sqrt{3}$
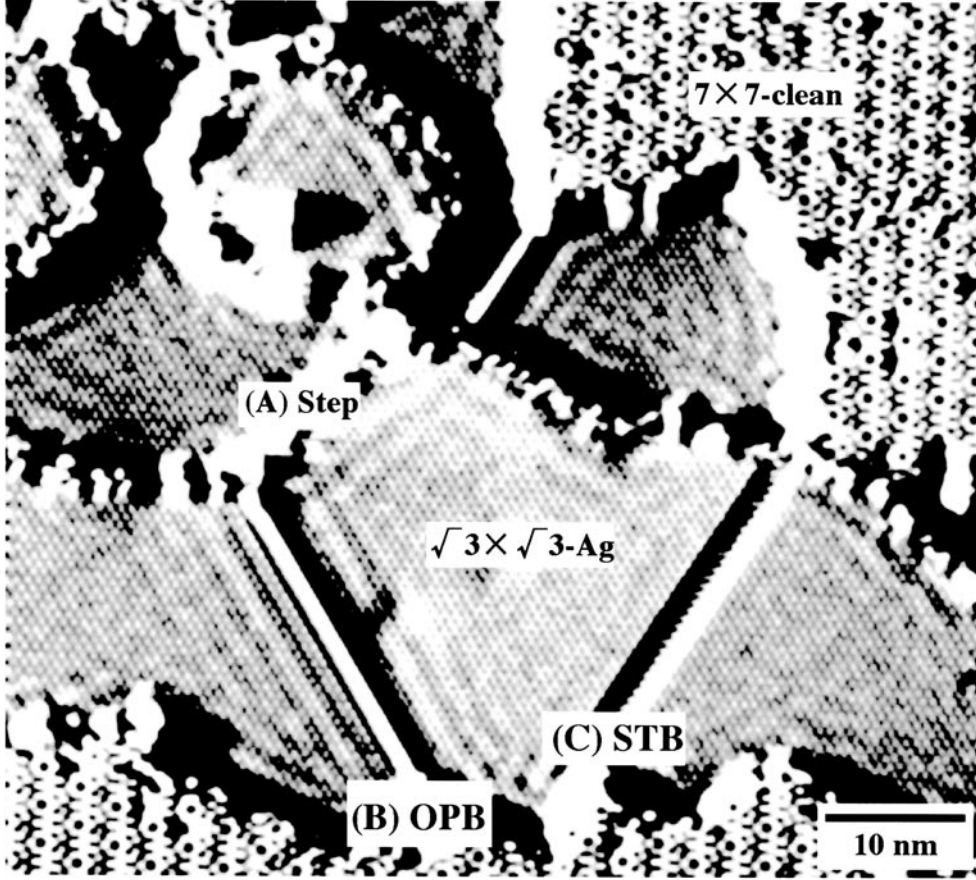
Figure 5. An empty-state STM image of the Si(111)–$\sqrt{3} \times \sqrt{3}$-Ag surface (the 7×7 structure partially remains) taken at 6 K. The tunnelling current is 0.18 nA with a sample bias of 1.0 V [42].

periodicity (as in figure 2(e)). Additionally, one can see standing-wave patterns superimposed near step edges (A) and domain boundaries (B). In a small domain shown on the upper right, surrounded by steps and domain boundaries, a complicated concentric interference pattern is observed, while near the straight domain boundaries, the interference patterns are parallel to the boundaries. There are no standing-wave patterns observable in the 7×7 domains.

These waves are interpreted as follows. Since the surface state S_1 has a parabolic band as shown in figure 4(a), its electron wavefunction can be described by a 2D Bloch wavefunction as

$$\Psi_i = u(x, y)e^{i(k_x x + k_y y)} \tag{3}$$

where $u(x, y)$ is the cell function representing the structure within the $\sqrt{3} \times \sqrt{3}$ unit cell. Its energy is written as

$$E = E_0 + \frac{\hbar^2(k_x^2 + k_y^2)}{2m^*} \tag{4}$$

where k_x and k_y are surface-parallel components of the wavevector, E_0 is the energy of the band bottom, and m^* is the effective mass of the surface-state electron. Domain boundaries and atomic steps, which are assumed to be straight in the y-direction, act as a potential barrier

for the surface-state electrons. So the electrons reflected from the barrier are expressed by

$$\Psi_r = R u(x, y) e^{i(-k_x x + k_y y)} \tag{5}$$

where the reflection coefficient $R = |R| e^{i\eta}$ with a phase shift η. Then, the local DOS $\rho(x, y; E)$ along the x-direction (perpendicular to the potential-barrier wall) can be written as

$$\rho(x, y; E) \propto |\Psi_i + \Psi_r|^2 \tag{6}$$

$$= \{1 + |R|^2 + 2|R| \cos(2k_x x - \eta)\} |u(x, y)|^2. \tag{7}$$

The standing waves in figure 5 come from the cosine term with a periodicity of π/k_x in real space, while the atomic corrugation originating from the surface superstructure comes from the term $|u(x, y)|^2$. They are superimposed in the image. The reflected and incident waves interfere with each other to make the standing waves.

Extending this consideration to 2D, the local DOS can be written as

$$\rho(x, y; E) \propto \{1 - J_0(k_\parallel x)\} |u(x, y)|^2 \tag{8}$$

$$\simeq \left\{ 1 - \frac{1}{\sqrt{\pi k_\parallel x}} \cos\left(2k_\parallel x - \frac{\pi}{4}\right) \right\} |u(x, y)|^2 \tag{9}$$

by assuming the step edge to be a hard wall (meaning complete reflection of the electron waves) [44], where J_0 is the zero-order Bessel function and its asymptotic formula is used, and $k_\parallel$ is the surface-parallel component of the wavevector.

On changing the bias voltage in STM imaging (in other words, by probing different energy levels), the wavelengths of the observed standing waves change according to a dispersion relation (E versus k_x) of the surface-state band [42] although the fine atomic corrugation remains unchanged. This is evidence for the wave patterns being due to the electronic nature, rather than geometric undulation. In this way, the $\sqrt{3} \times \sqrt{3}$-Ag surface is shown to have an extended surface electronic state, which will contribute to the electrical conduction parallel to the surface. But the carrier scattering by the step edges and domain boundaries is expected to be severe, as one would easily guess from the standing-wave pattern, resulting in a low carrier mobility. These transport properties due to the surface-state band will be described in section 5.

In contrast, the 7×7 clean surface has a surface-state band S_1 with negligible dispersion near E_F as shown in figure 4(d), which is known to come from dangling-bond states on the topmost Si atoms, and to make the main contribution to STM images. Its negligible dispersion means a localized nature, so standing waves are not expected, which also suggests a low conductivity along the surface through this surface state. This is indeed measured to be as low as of the order of 10^{-8} S/□ [45], which is much smaller than the surface-state conductivity of the $\sqrt{3} \times \sqrt{3}$-Ag surface—by about four orders of magnitude—as will be detailed in section 5.

The domain boundary (B) in figure 5 is a conventional out-of-phase boundary (OPB) due to phase mismatch in the super-periodicity between the adjacent domains [6, 38], which is shown in detail in figures 6(a), 6(b), while the boundary (C) in figure 5 is a 'surface twin boundary' (STB) (figures 6(c), 6(d)) which appears only at low temperatures below the symmetry-breakdown transition. At the STB (C) in figure 5, no standing waves are observed. In other words, the STBs are transparent to the surface-state electrons. Then, an important and interesting question is raised here: what is the transmission coefficient of the electron wavefunction at the step edges and domain boundaries? Although some papers assumed the step edge to be a hard wall for the surface-state electrons, meaning a transmission coefficient of zero [44, 46–49], this should be questioned, because it governs an important parameter, the mobility of surface-state carriers. It is certain from figure 5 that carrier scattering by the step
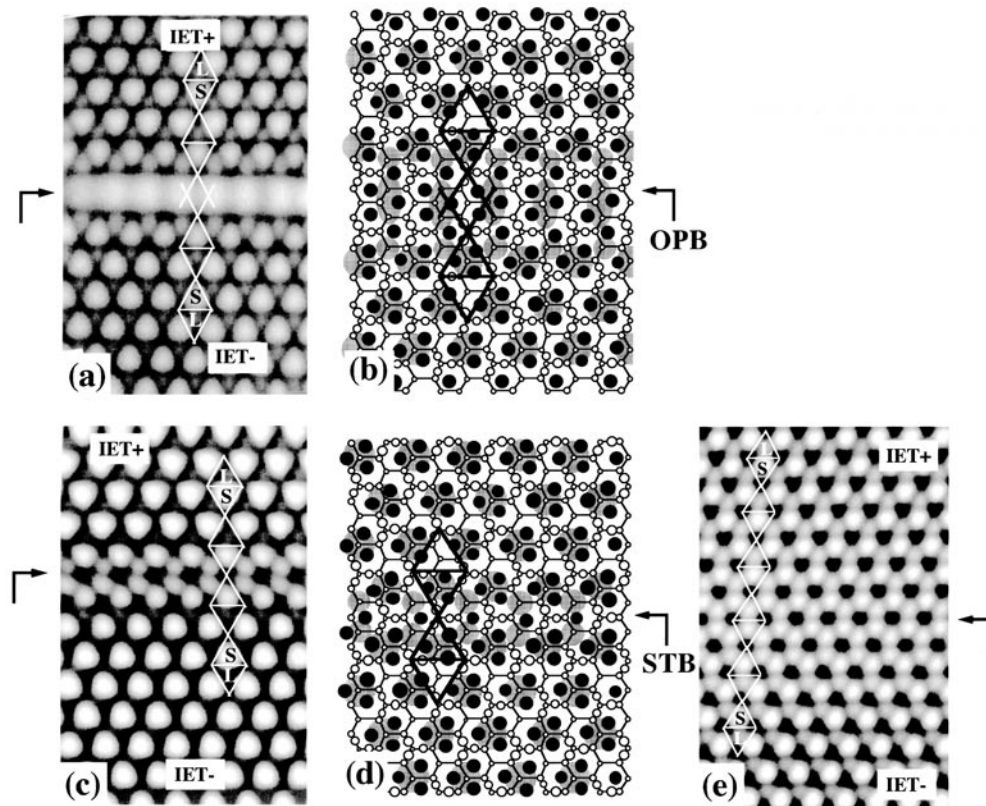
Figure 6. STM images ((a), (c), (e)) and schematic diagrams ((b), (d)) of boundaries between two types of domain on the Si(111)-$\sqrt{3} \times \sqrt{3}$-Ag surface: ((a), (b)) out-of-phase boundaries (OPBs); and ((c), (d), (e)) surface twin boundaries (STBs). IET+ and IET− indicate two types of domain in a twinning relationship where the symmetry breakdown occurs in opposite ways. (c) shows a sharp STB at which IET+ changes into IET− abruptly, while (e) shows a broad STB where the symmetry gradually changes. The STBs exhibit the honeycomb-lattice pattern just like the HCT structure.

edges and domain boundaries lowers the carrier mobility. But by how much is it lowered? The mobility of the surface-state electrons on the $\sqrt{3} \times \sqrt{3}$-Ag surface is actually measured to be lower than that in the bulk crystal by two orders of magnitude [50].

The surface-space-charge layers below the surfaces are also very different for the 7×7 and $\sqrt{3} \times \sqrt{3}$-Ag surface superstructures as shown in figures 4(b) and 4(e): a depletion layer below the 7×7 structure, but a hole-accumulation layer beneath the $\sqrt{3} \times \sqrt{3}$-Ag structure. Therefore, the electrical conductivities through the subsurface region are also expected to be different for these superstructures. Such surface transport properties will be discussed in section 5.

3.3. The plasmon in the surface-state band

By analogy with oscillations of the electron density in bulk metals, plasmons, excited by irradiation of charged particles or electromagnetic waves, plasmons in the metallic surface-state band S_1 are expected on the $\sqrt{3} \times \sqrt{3}$-Ag surface. These *surface-state plasmons* should

be distinguished from surface plasmons which are charge oscillations due to 3D electron gas at the edge of a semi-infinite bulk metal.

To detect such plasmons, electron-energy-loss spectroscopy (EELS) is employed, in which monochromatic low-energy electrons irradiate the sample surface, and energy distributions of the scattered electrons are measured in selected detection directions much like in ARPES.

Figure 7 shows typical EELS spectra taken from the $\sqrt{3} \times \sqrt{3}$-Ag surface by irradiating with an electron beam of 12.4 eV energy [20], changing the detection angle. A single loss feature is clearly seen, dispersing up to around 600 meV. From such data, dispersion plots (energy versus wavevector) of the excitation were constructed. The dispersion relations thus obtained were independent of the doping type/concentrations in bulk Si crystals and also of the
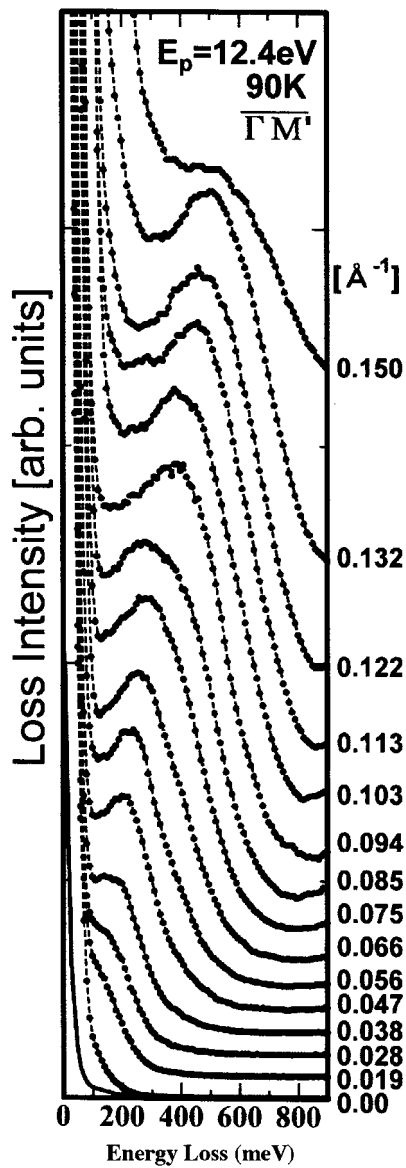

Figure 7. Electron-energy-loss spectra taken from the $\sqrt{3} \times \sqrt{3}$-Ag surface at 90 K at different detection angles along the Γ–M direction in the $\sqrt{3} \times \sqrt{3}$-surface Brillouin zone [20].

primary energies of the electron beam. This means that the observed loss does not have any origin in the surface-space-charge layer or in the bulk. Elaborate measurements and analyses of the dispersion and damping of the loss features in the spectra lead to the conclusion that the observed excitation is unambiguously the plasmon in the 2D free-electron-like surface-state band S_1. This is the first experimental evidence of surface-state plasmons. The electron density derived from the plasmon dispersion was consistent with that of the S_1 band in the 2D band dispersion diagram of figure 4(a) [20].

4. Quasi-one-dimensional metal; the Si(111)–4 × 1-In surface

Let me introduce another surface superstructure. When one ML of indium atoms adsorb on a Si(111) surface at around 300 °C, the Si(111)–4 × 1-In surface superstructure is formed. But its atomic arrangement is not yet confirmed [51]; figure 8 shows the model most recently proposed, based on x-ray diffraction analysis [52]. Indium atoms arrange in four lines along the [1$\bar{1}$0] direction, between which zigzag Si chains run. These atomic chains are seen as stripes in the STM image of figure 9(a) taken at RT. Each stripe corresponds to the four In chains, aligned with a spacing corresponding to the four-times super-periodicity. Along each stripe, one can see fine corrugations corresponding to the fundamental periodicity. Thus, the 4 × 1 unit cell is confirmed by the image, although the atomic arrangements in the unit cell are not resolved.

As one can imagine from the STM image, the surface electronic state is very anisotropic. According to an ARPES study by Abukawa *et al* [53], it is metallic along In chains, while it is insulating in the perpendicular direction. Their results are summarized in the band dispersion diagram in figure 10(a). Along the indium chains (k_x-direction), one can find three dispersive bands, m_1, m_2, m_3, all of which cross E_F, indicating metallic bands. On the other hand, along the k_y-direction perpendicular to the chains, these bands show no significant dispersion. This indicates that the electrons in these bands are mobile along the stripes in figure 9(a), while it is hard to make them hop to the neighbouring stripes, i.e., this is a one-dimensional metal. This nature is also confirmed for unoccupied states revealed by inverse photoemission spectroscopy [54].

One can find another interesting feature in figure 10(a); the m_3 band crosses E_F at around the middle of the surface Brillouin zone, and its Fermi surface (line) is roughly parallel to the k_y-direction, as shown in figure 10(b). This means that a nesting vector of $2k_F$ exists along the indium chains (k_F is the Fermi wavenumber). Therefore, one can expect the formation of charge-density waves with double periodicity due to the Peierls instability of one-dimensional metals.

Then the surface was cooled down [55]. As expected, modulations (ripples) with the double periodicity were actually observed! Figure 9(b) is an STM image of the 4 × 1-In surface taken at 70 K, showing the modulations on each stripe clearly. Then, the periodicity becomes 4 × 2 (though its actual periodicity turned out to be 8 × 2, from electron diffraction measurements, probably because of an inter-chain interaction). The ripples are not so clear on some stripes in figure 9(b), which is due to some fluctuation. One can notice furthermore that the ripples on some neighbouring stripes are out of phase. Then, can we say that these ripples are the charge-density waves due to the Peierls instability, as expected?

Since electron diffraction from this low-temperature phase showed double super-periodicity along the indium chains [55], the lattice is also modulated with the double periodicity. According to the most recent x-ray diffraction investigation [56], indium atoms shift slightly at low temperatures to produce the doubled periodicity caused by indium trimers positioned alternately in each stripe. Moreover, ARPES measurements at low temperature
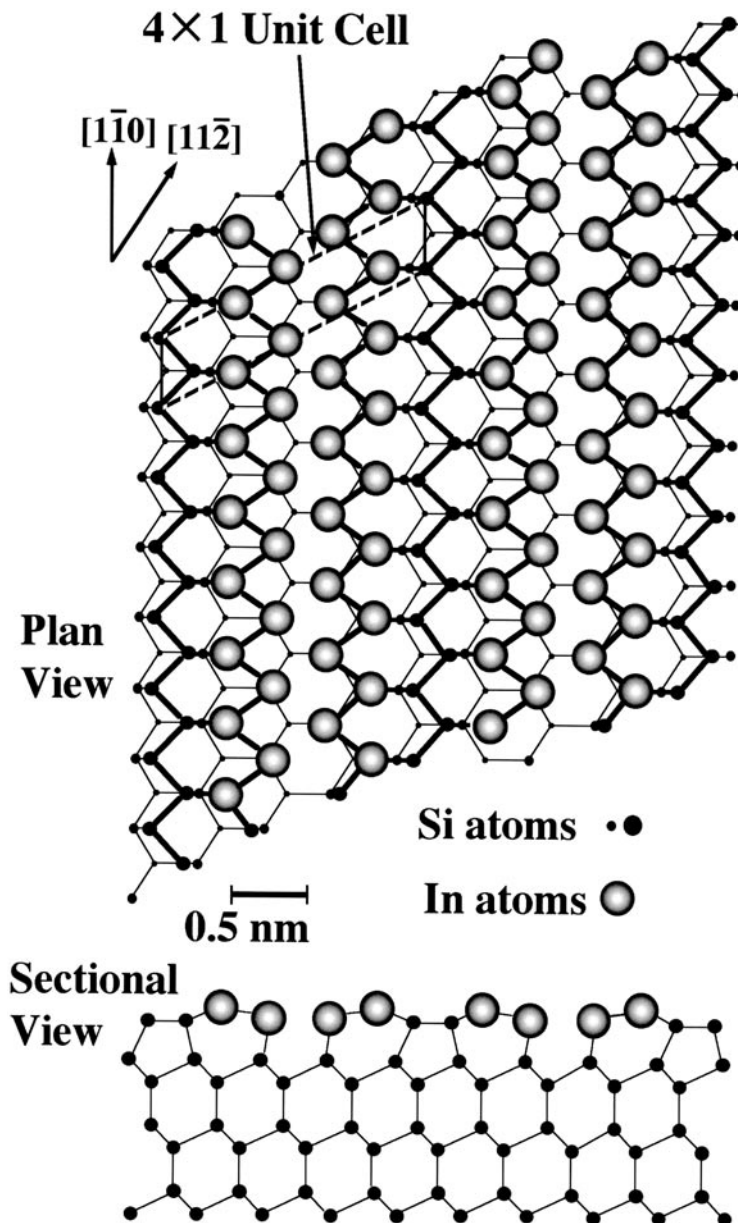
4×1 Unit Cell

[1̄10] [112̄]

Plan View

Si atoms ·●
In atoms ○

0.5 nm

Sectional View

Figure 8. A model of the atomic arrangement of the Si(111)–4 × 1-Ag surface [52].

show that the metallic states shown in figure 10(a) lose their spectral weight at E_F, showing a semiconducting nature. This means that a metal-to-nonmetal transition occurs on cooling. In this way, the experimental findings of a nesting vector in the Fermi surface, lattice distortion, and electronic changes at E_F indicate that the 4 × 1-In surface should undergo a Peierls transition upon cooling, accompanying the charge-density waves observed in figure 9(b) [55]. Although Peierls transitions are known to occur in quasi-1D organic bulk materials [57, 58], that for the 4 × 1-In surface represents the first case in surface-state bands.
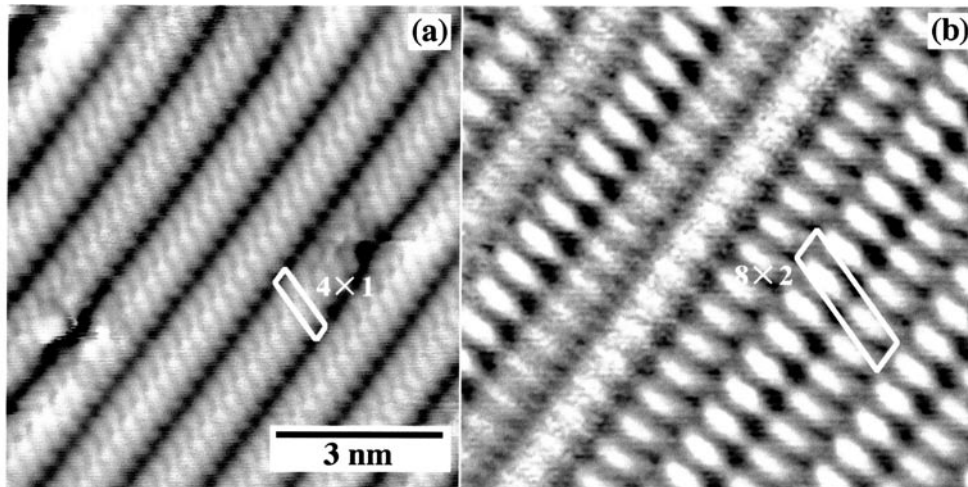
Figure 9. Empty-state STM images of the Si(111)–4 × 1 surface (a) at room temperature and (b) at 70 K. The tunnelling current was 0.2 nA with a bias voltage of 1.0 V [55].

Another interesting point for possible future study as regards this surface superstructure is the non-Fermi-liquid behaviour. A 1D metal might be a Tomonaga–Luttinger liquid due to a strong electron correlation effect [59]. The reduction of the spectral weight at E_F observed at low temperatures might be a signature of this character [60].

5. Electronic transport through surface-state bands

So far, I have described various phenomena in which surface electronic states play main roles, which are directly observed by STM and other surface-sensitive techniques. Now, I come to the point of discussing electronic transport through the surface states. Although some efforts have been devoted since the 1960s to detecting the surface-state electrical conduction parallel to the surface [61], which should be distinguished from the conduction through bulk states in surface-space-charge layers, it is only very recently that the surface-state conduction has been experimentally detected unambiguously [4]. I will show this by using the Si(111)–$\sqrt{3} \times \sqrt{3}$-Ag surface, which readers are already familiar with from section 3.

5.1. Four-point-probe measurements in ultra-high vacuum

When two electrical leads (e.g., outer probes in linear four-point-probe measurements as illustrated in figure 11(a)) are connected to a surface of a semiconductor crystal with a macro-scopic spacing, and when a voltage is applied between them, a current I flows through three channels on/in the specimen crystal [61]:

(1) surface-state bands on the topmost atomic layers (when a well-ordered surface super-structure is formed on the surface),
(2) bulk-state bands in a surface-space-charge layer beneath the surface (when bands bend enough), and
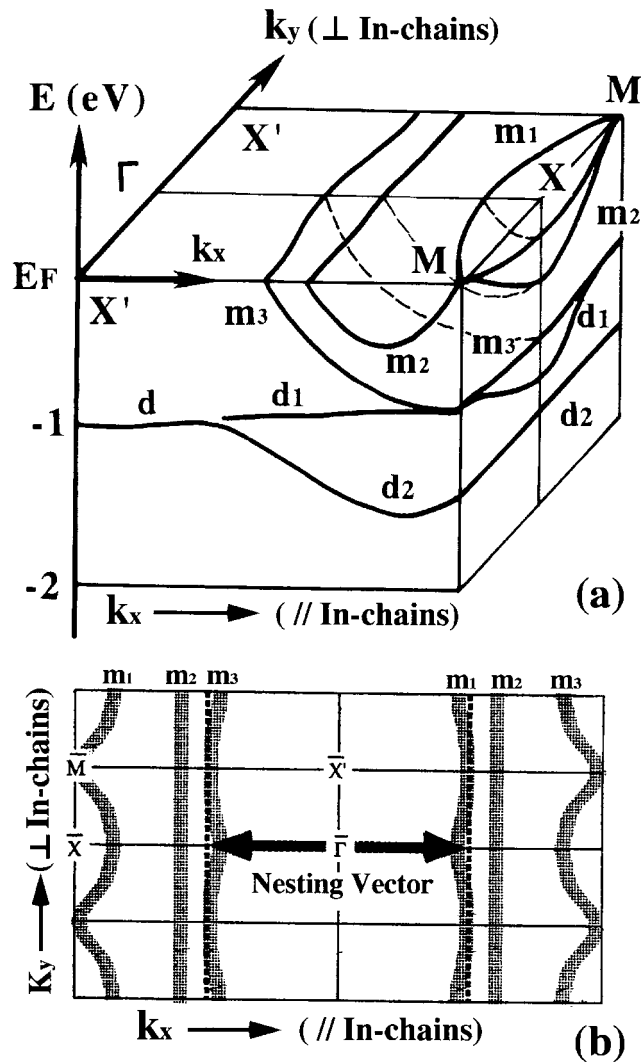(3) huge bulk-state bands in the inner crystal (independent of the surface conditions and treatments).

Figure 10. Surface-state bands of the Si(111)–4 × 1-In structure, determined by ARPES at RT [53]. k_x and k_y are the components of wavevector along the indium chains and perpendicular to them, respectively. (a) The band dispersion is drawn three dimensionally. (b) The Fermi surface in the surface Brillouin zone.

A voltage drop V is measured by a pair of inner probes in figure 11(a) to obtain a four-point-probe resistance $R = V/I$ (with a geometrical correction factor), which contains the contributions from all of the above three channels. This four-point-probe method avoids contact resistances at the probe–sample contacts to give the sample resistance only, irrespective of whether the contacts are of ohmic or Schottky type. But it is impossible to separate the contributions of the above three channels. Under usual conditions in air, without surface superstructures on the surface, the measured resistance is interpreted as a bulk resistance. However, when bulk bands bend steeply beneath the surface to make an electron- or hole-accumulation layer (surface-space-charge layer), or when conductive surface-state bands are created due to well-ordered surface superstructures in ultra-high vacuum (UHV), the
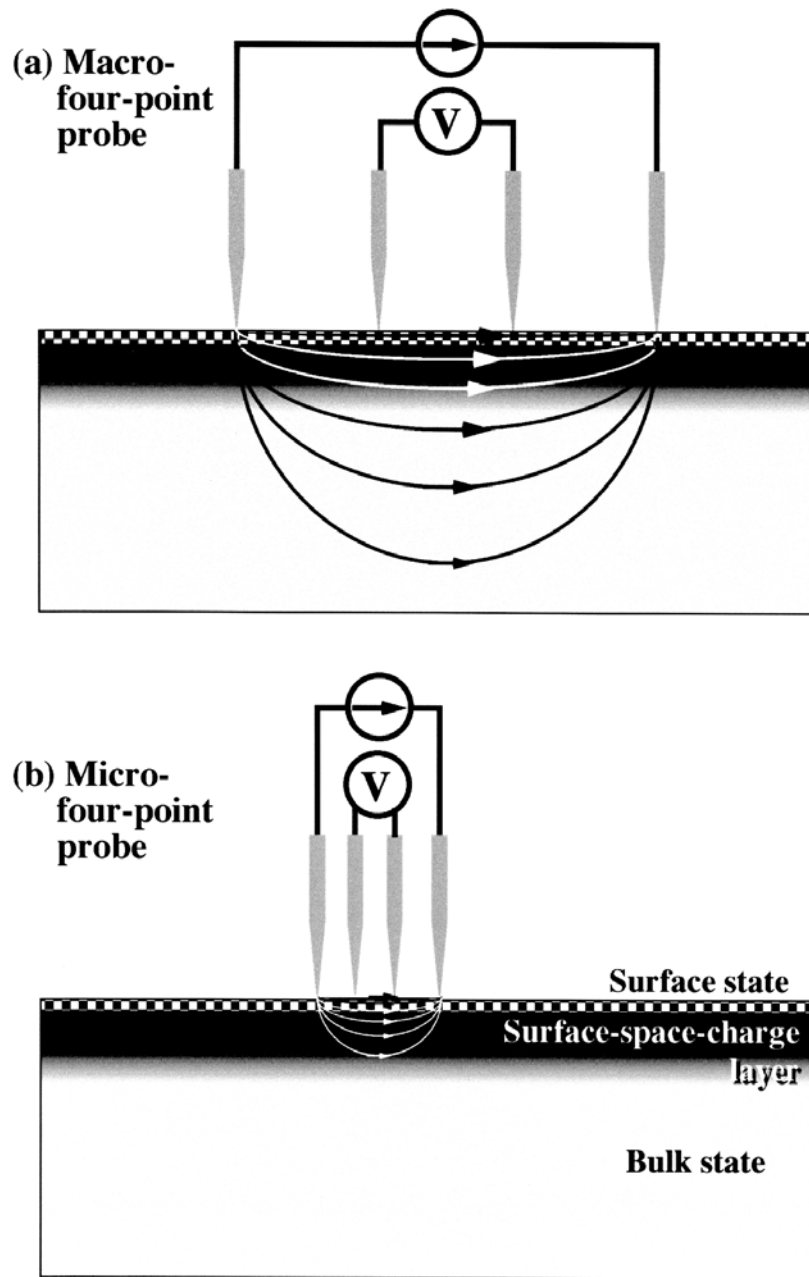
Figure 11. Linear four-point probes on (a) macroscopic and (b) microscopic scales, with schematic illustrations of current paths near the semiconductor surface.

conductivity of the space-charge layers or surface-state bands cannot be ignored in the measured resistance. However, even in such cases, the surface-layer contributions are considered to be quite small because a large fraction of the current tends to flow through the interior bulk as illustrated in figure 11(a) when the probe spacing is a macroscopic distance. But it does work

for detecting the conductance of the surface-state bands, as described below. The microscopic-scale studies shown in figure 11(b) will be discussed in section 6.

The sample holder actually used in UHV for *in situ* conductance measurements is illustrated in figure 12; it enables metal depositions and RHEED observations to be carried out simultaneously to prepare well-defined surface superstructures on the whole surface [4, 62]. After the superstructures have been prepared, a small direct current is fed into the specimen crystal through the end clamp electrodes, and the voltage drop is measured between a pair of Ta-wire contacts to obtain the resistance of the central part of the crystal. The spacing of the probe contacts is usually as large as about 10 mm.
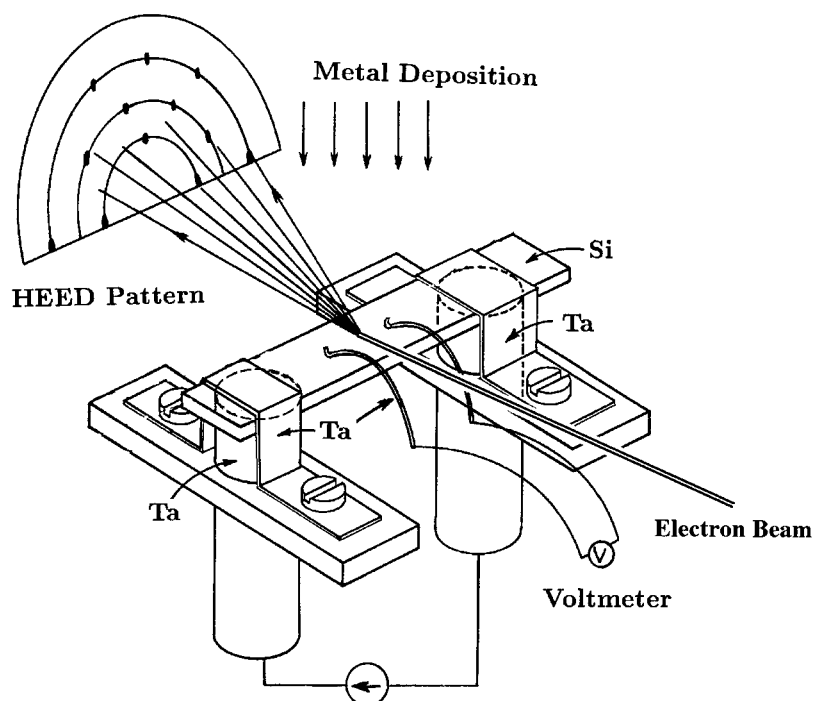

Figure 12. A RHEED sample holder for *in situ* electrical conductivity measurements in UHV using a 'four-point-probe' method. After the surface superstructures are confirmed by using RHEED, the electron beam is always turned off during the subsequent conductivity measurements.

By comparing the resistances measured in this way for the 7×7 clean surface and for the $\sqrt{3} \times \sqrt{3}$-Ag surface of the same crystal, it is found that the latter surface has a smaller resistance, by about 15%, than the former one (for a Si crystal having the resistivity of 50 Ω cm at RT). This result should be surprising, because the 15% difference in resistance might be very large if one considers the thickness of the Si crystal, 0.4 mm, in which more than one million atomic layers are stacked: the difference in atomic arrangement in only one or two atomic layers at the surface of the one million layers induces a 15% change in resistance! But, strictly speaking, the relative change in resistance depends on the doping concentration in the bulk; a physically meaningful quantity is the sheet conductance. By converting the measured resistances R into the sheet conductances using $\sigma = (L/W)(1/R)$ (L is the probe spacing and W the crystal width), it is found that the $\sqrt{3} \times \sqrt{3}$-Ag surface has a higher sheet conductance than the 7×7 clean surface by approximately 1×10^{-4} S/$\square$, irrespective of the bulk doping concentration.

In this way, a higher conductance for the $\sqrt{3} \times \sqrt{3}$-Ag surface is confirmed, as expected. Then, can one conclude that this excess conductance comes from the free-electron-like surface-state band S_1 introduced in section 3? Unfortunately, the nature is not so straightforward. It is already known from core-level photoemission spectroscopy measurements that the bulk bands bend upward steeply, as shown in figure 4(b), beneath the $\sqrt{3} \times \sqrt{3}$-Ag superstructure, so excess holes are induced in the bulk valence band to make a surface-space-charge layer [63]. On the other hand, the layer below the 7×7 clean surface is a depletion layer (figure 4(e)) [2,3]. Then, the conductance through the subsurface regions should be different. Once the E_F-positions at the surface and in the bulk are known, the surface-space-charge-layer conductance of the respective surfaces can be calculated by an established method for semiconductor devices [64]. It is found that the difference between the calculated conductances almost coincides with the measured difference. As a conclusion, then, we can say that the detected excess conductance of the $\sqrt{3} \times \sqrt{3}$-Ag surface comes from the surface-space-charge layer, not from the surface-state band S_1 as we had initially hoped [65]. This is a very disappointing result.

5.2. Adsorbate-induced conductance changes

But this is not the end. One of the unambiguous ways to detect the surface-state conductivity is to measure a conductance change induced by a perturbation only of the surface states. We measured the resistance changes of the $\sqrt{3} \times \sqrt{3}$-Ag surface at RT during intermittent deposition of small amounts of additional Ag atoms on it [66]. The result is shown in figure 13(a); only 0.008 ML of Ag were deposited in each period of about 2 s, which caused resistance drops as large as 10%. After interrupting the depositions by closing an evaporator shutter, the resistance remained constant during the interval A. This indicates that the observed resistance drop is not due to thermal irradiation from the evaporator, but is rather due to the Ag adsorption. On re-starting the deposition of 0.008 ML, the resistance further decreased, and it remained the same again on interrupting the deposition (interval B). These changes in resistance were observed up to an additional Ag coverage of about 0.03 ML in total (the critical coverage). Do the deposited Ag atoms align to make conductive paths on the surface?—No. The amount, 0.03 ML, is too small for making percolation paths; the critical coverage for percolation on a triangular lattice is 0.5 ML [67]. We focus here on the very early stages indicated by A, B, and C in figure 13(a) (the later stages marked D, E, and F will be discussed in subsection 5.5).

Some changes in electronic states near the surface should be induced by the adsorption of small amounts of Ag. First, we investigated the change in number of the excess holes in the surface-space-charge layer beneath the $\sqrt{3} \times \sqrt{3}$-Ag surface which was mentioned in connection with figure 4(b). In other words, the band bending below the surface was measured by the Si 2p core-level shift in the x-ray photoemission spectra taken in the bulk-sensitive mode. Then, it turned out that the small amount of Ag adatoms made the core level shift toward the higher-binding-energy side. In other words, the bending of bulk bands beneath the surface changes toward the flat-band condition. This means that the hole-accumulation layer beneath the initial $\sqrt{3} \times \sqrt{3}$-Ag surface becomes a depletion layer, as shown in the left-hand inset of figure 13(b), resulting in a *decrease in conductivity through the surface-space-charge layer*. Therefore, the observed resistance drop in figure 13(a) cannot be understood on the basis of the surface-space-charge-layer conductivity.

5.3. Surface-state conduction

Next, we made ARPES measurements for valence bands from the $\sqrt{3} \times \sqrt{3}$-Ag surface covered by excess Ag adatoms to a depth of 0.022 ML, which nearly corresponded to the situation in

the interval C in figure 13(a). The spectra obtained were almost the same in shape as the ones for the 'clean' $\sqrt{3} \times \sqrt{3}$-Ag surface shown in figure 3 ('clean' means no excess Ag adatoms on the surface). But the whole spectra shifted in energy toward the higher-binding-energy side compared with those in figure 3. This change is shown as a downward shift of the surface-state bands in the 2D dispersion diagram as shown in figure 13(b); all of the S_1, S_2, and S_3 bands shift down (from open circles to filled circles) in parallel by about 0.15 eV upon adsorption of 0.022 ML of Ag adatoms (the data indicated by crosses will be discussed later in subsection 5.5). The extent of the shift is approximately equal to that of the above-mentioned Si 2p core-level shift. Due to this downward shift in energy, the Fermi disk made of the S_1 surface-state band grows, as shown in the right-hand inset of figure 13(b), indicating an increase in the number of electrons in this band, from 1.6×10^{13} e$^-$ cm^{-2} to 3.5×10^{13} e$^-$ cm^{-2}. This leads to the increase in number of conduction electrons. This is the reason for the observed resistance drops in figure 13(a). In this way, the electrical conduction through the surface-state band is experimentally detected [50].

Some readers may still doubt me. 'Your Si crystal could be as thick as 0.4 mm, and you measured the resistance of the whole crystal, not the surface region only, as shown in figure 11(a). Therefore the measured resistance dominantly reflects the bulk value, so the resistance change that you observed in figure 13(a) should be dominated by a change in the bulk. It is overhasty to attribute the observed resistance drops to just the surface-state conduction.'—But it is very unlikely that the adsorption of only 0.022 ML of Ag adatoms induces a conductance change in the bulk crystal deeper than the surface-space-charge layer. The solubility of Ag atoms in Si is negligibly small, and furthermore Ag will not diffuse into the bulk Si crystal at RT. The influence of the adatom adsorption on the surface will extend through a region equal to the Debye length below the surface at most, i.e., only to the surface-space-charge layer. The deeper region will not be affected by the adsorption. Therefore, we must conclude that the *change* in resistance shown in figure 13(a) results from some changes in the surface region only. The surface region contains both the surface-space-charge layer and surface-state bands. In the present case, fortunately, the surface-state band alone dominates the observed resistance change. Such surface-state conductivity will be more clearly described in the following sections.

5.4. Carrier doping into surface-state bands

As shown in figure 13(b), the number of electrons in the surface-state band S_1 increases on additional Ag adsorption on top of the $\sqrt{3} \times \sqrt{3}$-Ag surface. Then, where do the electrons come from? They should not come from the substrate bulk, because the surface-space-charge layer turns into a depletion layer from an initial hole-accumulation layer (left-hand inset in figure 13(b)), meaning that the substrate also accepts some electrons to compensate the holes; the bulk cannot provide electrons to the surface-state band. Then, we must say that the excess electrons accumulated in the surface-state band S_1 (and also in the surface-space-charge layer) come from the adsorbed Ag adatoms. That is, the adsorbed Ag adatoms act as donors to provide electrons to the substrate. The adatoms themselves become positively charged, which is consistent with the conclusion of electromigration of Ag atoms on the $\sqrt{3} \times \sqrt{3}$-Ag surface, showing a positive charge of the migrating Ag adatoms [68]. Moreover, the downward shift of the band bending shown in the left-hand inset in figure 13(b) is also consistent with a positive charge of the Ag adatoms (or decrease in negative-charge density on the surface). By comparing the Ag-adatom density and the number of electrons doped into both the S_1 band and the surface-space-charge layer, each Ag adatom is found to provide approximately one electron from its valence orbital [4, 40, 50]. The increase in number of electrons in the S_1 band
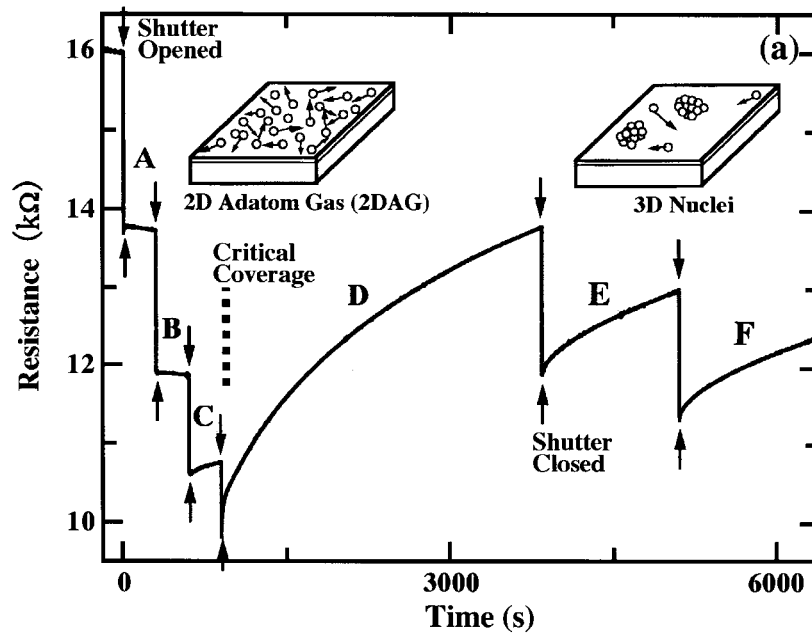
Figure 13. (a) The resistance change of a Si wafer during intermittent Ag depositions (rate = 0.24 ML min^{-1}) onto the Si(111)–$\sqrt{3} \times \sqrt{3}$-Ag surface at RT. The Si wafer is an n-type one of 100 Ω cm resistivity. Downward-pointing arrows indicate the starting points of depositions, and upward-pointing arrows their end points. Ag atoms to a depth of 0.008 ML are deposited during each deposition period (two seconds). A–F indicate the interruption intervals. (b) A two-dimensional band dispersion diagram of the S_1, S_2, and S_3 surface states for the three samples; the initial $\sqrt{3} \times \sqrt{3}$-Ag surface (open circles), the same surface covered with a two-dimensional adatom gas (2DAG) of 0.022 ML Ag (filled circles), and the same surface covered with 3D nuclei of 0.088 ML Ag (crosses). The spectra were recorded in the [01$\bar{1}$] direction, corresponding to the $\bar{\Gamma}$–$\bar{M}$–$\bar{\Gamma}$ direction in the $\sqrt{3} \times \sqrt{3}$-surface Brillouin zone [50]. Thin solid lines are only to guide the eye. Left-hand inset: the change in band bending due to the 2DAG adsorption. Right-hand inset: the change in the Fermi disk due to the 2DAG adsorption.

caused by additional Ag adsorbates is also detected as a change in dispersion relation of the surface-state plasmon mentioned in section 3 [20].

The increase of electron density Δn in the surface-state band S_1 can be estimated from the band diagram of figure 13(b) by assuming its isotropic dispersion. The conductance increase $\Delta\sigma$ is estimated from the measured resistance drop in figure 13(a). Then, from the relation

$$\Delta\sigma = e\mu\,\Delta n \tag{10}$$

(e is the elementary charge), we can estimate the mobility μ of the surface-state electrons to be of the order of 10 cm^2 V^{-1} s^{-1}. This value is lower than the electron mobility in bulk Si crystals by about two orders of magnitude. This low mobility may be seen to be reasonable when one considers the severe carrier scattering by phonons because of the strict two dimensionality of the surface-state band, and also carrier scattering by defects such as steps and domain boundaries on the surface which is actually observed in figure 5 as electron standing waves. In order to clarify the mechanism of carrier scattering in surface-state bands quantitatively, the temperature dependence of the conductivity must be measured, which has not yet been done. By measuring the surface-state conductivity with microscopic four-point probes (the probe spacing being 8 μm) as shown in figure 11(b) to avoid the surface steps, which will be
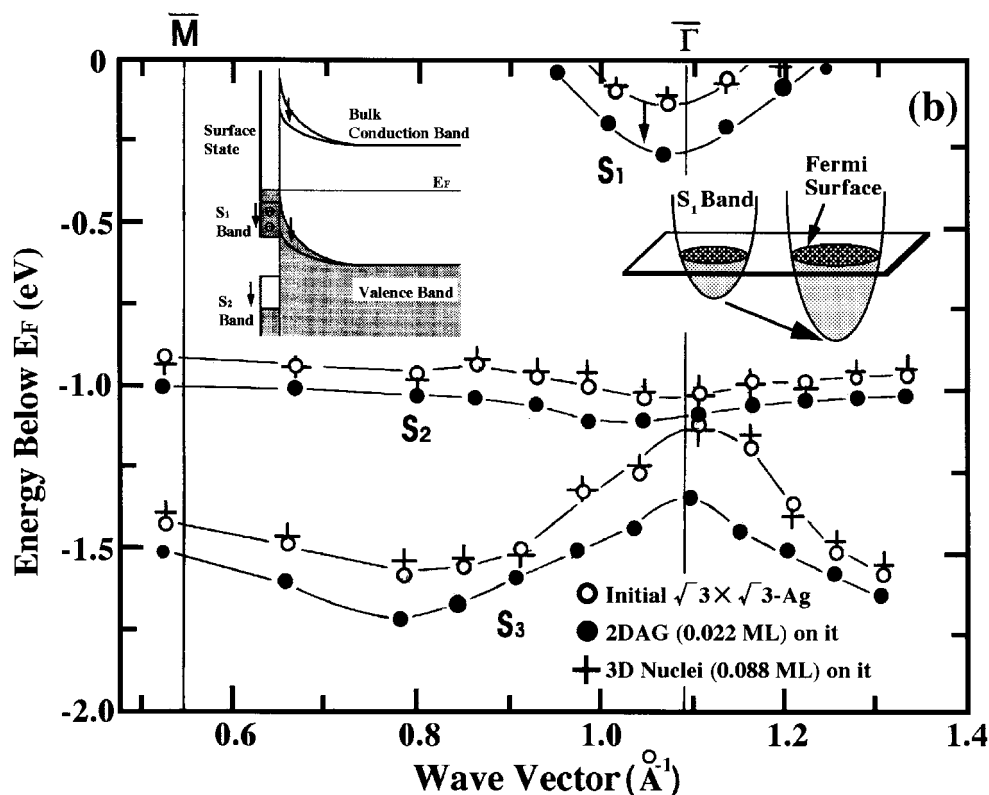
Figure 13. (Continued)

described in section 6, the mobility was increased by nearly one order of magnitude. This really shows that the apparent low mobility estimated above according to the macroscopic four-point-probe measurements results from the carrier scattering at step edges and domain boundaries.

5.5. Two-dimensional adatom gas (2DAG)

As described in connection with figure 13(a), the small amounts of Ag adatoms deposited on the $\sqrt{3} \times \sqrt{3}$-Ag surface at RT have an electron-doping action. But such Ag adatoms are not observable by STM, because they migrate on the surface very rapidly at RT to make a '2D adatom gas (2DAG)' phase [66]. But on cooling the substrate to far enough below RT to reduce and freeze the adatom migration, such adatoms become observable [28]. In figure 14(a), at 6 K, individual adatoms are completely frozen, making star-like protrusions in STM images, while at 65 K, in figure 14(b), they have already been made mobile by the STM tip during scanning. At RT, they must migrate too fast to be observed. They adsorb on the surface individually as monomers, as seen in figure 14(a), and do not aggregate into clusters at RT. This is why we call them a 2DAG phase.

However, beyond about 0.03 ML coverage, the Ag adatoms begin to nucleate. This is similar to mist formation in air in which the humidity must exceed the saturation vapour pressure to lead to water drops in air. Such a nucleation process is detected as a resistance rise in figure 13(a). Once stable nuclei are formed beyond the critical coverage (critical
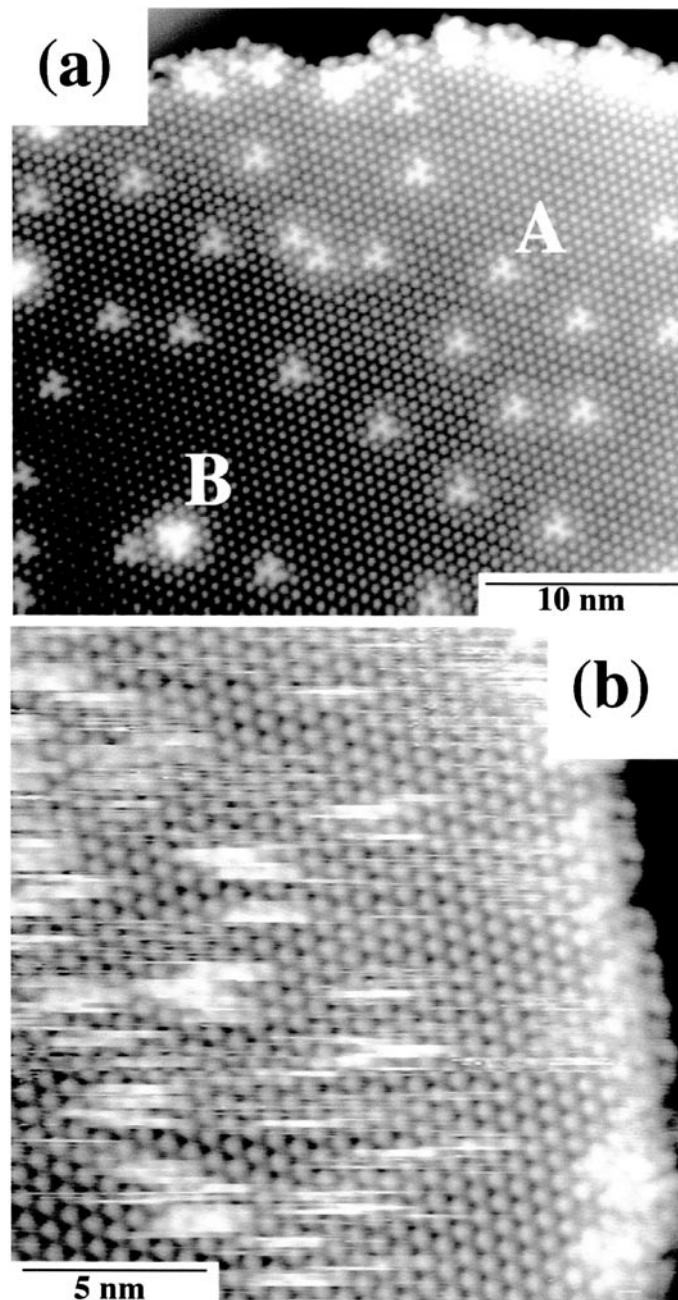
Figure 14. A two-dimensional adatom gas (2DAG) of Ag on top of the Si(111)–$\sqrt{3} \times \sqrt{3}$-Ag surface (a) frozen at 6 K and (b) migrating at 65 K [28]. Star-like protrusions indicated by A are assumed to be single Ag adatoms because they are the minimum units observed, while a cluster indicated by B is thought to be composed of three Ag adatoms.

supersaturation) of the adatom gas, the resistance steeply increases toward the initial value during the interruption periods D, E, and F in figure 13(a). This corresponds to a process

where the deposited Ag adatoms are swiftly captured by the stable nuclei, with the result that the density of isolated adatoms in the 2DAG phase is reduced down to a lower equilibrium vapour pressure [69]. In other words, below 0.03 ML coverage (interruption periods A, B, and C), the 2DAG is supersaturated; its supersaturation is about as large as 10, probably because of electrostatic repulsion among the ionized Ag adatoms due to the carrier-doping action. The stable nuclei or 3D islands of around 10 nm size are actually observed by SEM [66]. Once the Ag adatoms are incorporated into the islands, they lose the electron-doping action, which is shown in figure 13(b) in which, as indicated by crosses, the bands shift back to the initial energy position due to the 0.088 ML deposition of Ag adatoms (more than the critical coverage). This also occurs because the density of the isolated adatoms in the 2DAG phase, which act as electron donors, is greatly reduced by the 3D nuclei formation compared with the supersaturated situation. Therefore, the Fermi disk made of the S_1 surface-state band shrinks to the initial one. This is why the resistance increases on interrupting the Ag deposition. During this process, the band bending beneath the surface was found to return to the initial hole-accumulation condition from the depletion condition with the 2DAG on the surface, which is opposite to the change expected from the resistance increase. The manner in which the resistance increases, e.g. by the process illustrated in figure 13(a), should provide some information about the atomistic nucleation process of the deposited atoms [4, 66].

The carrier doping into the surface-state band by the adatoms in the 2DAG phase described above is similar in a sense to the carrier doping into the 2D conductive CuO_2 plane by Y atoms, for example, in high-T_C superconductors such as YBaCuO crystals.

Such a doping action for the surface-state band on the $\sqrt{3} \times \sqrt{3}$-Ag surface, increasing the conductivity, is not limited to Ag adatoms; small amounts of other noble-metal adatoms (Au and Cu) and alkali-metal adatoms (K, Na, and Cs) are also found to induce similar phenomena on the $\sqrt{3} \times \sqrt{3}$-Ag surface [41, 70, 71]. The common feature of these adatoms is monovalency; they tend to easily donate a valence electron. These monovalent-metal adatoms act as donors for the S_1 surface-state band, increasing the carrier concentration and leading to an increase of the surface-state conductivity [71].

In contrast, none of the divalent and trivalent adatoms such as Ca, Mg, In, or Ga on the $\sqrt{3} \times \sqrt{3}$-Ag surface induced any conductance increases; their adsorptions reduce the conductance by destroying the $\sqrt{3} \times \sqrt{3}$-Ag structure [72].

5.6. $\sqrt{21} \times \sqrt{21}$ surface superstructure

Another example is known showing the surface-state electrical conduction unambiguously. As briefly mentioned above, small amounts (less than 0.1 ML) of Au adatoms adsorb as a 2DAG phase on top of the $\sqrt{3} \times \sqrt{3}$-Ag surface at RT, and act as donors, increasing the surface-state conductivity, as in the case of Ag adatoms [41]. On increasing the coverage, while the Ag adatoms just nucleate into 3D islands without wetting the substrate, the Au adatoms begin to nucleate two dimensionally to make domains with a new order, $\sqrt{21} \times \sqrt{21}$ surface superstructure, as shown in figure 15. In correspondence with the $\sqrt{21} \times \sqrt{21}$ phase covering the entire surface at Au coverage of around 0.2 ML, the conductivity increases remarkably as shown in figure 16(a). On depositing Au beyond the 0.2 ML coverage, the $\sqrt{21} \times \sqrt{21}$ superstructure converts into another type of $\sqrt{3} \times \sqrt{3}$ phase consisting of an Ag and Au mixture. Then, the conductivity steeply decreases. Therefore it can be said that only the $\sqrt{21} \times \sqrt{21}$ phase is highly conductive.

As shown in figure 16(c), Cu adsorption of around 0.1–0.15 ML coverage on the $\sqrt{3} \times \sqrt{3}$-Ag surface at RT also induces a similar $\sqrt{21} \times \sqrt{21}$ phase. When Ag is deposited onto the $\sqrt{3} \times \sqrt{3}$-Ag surface below 250 K, Ag adsorption also induces a similar $\sqrt{21} \times \sqrt{21}$ phase
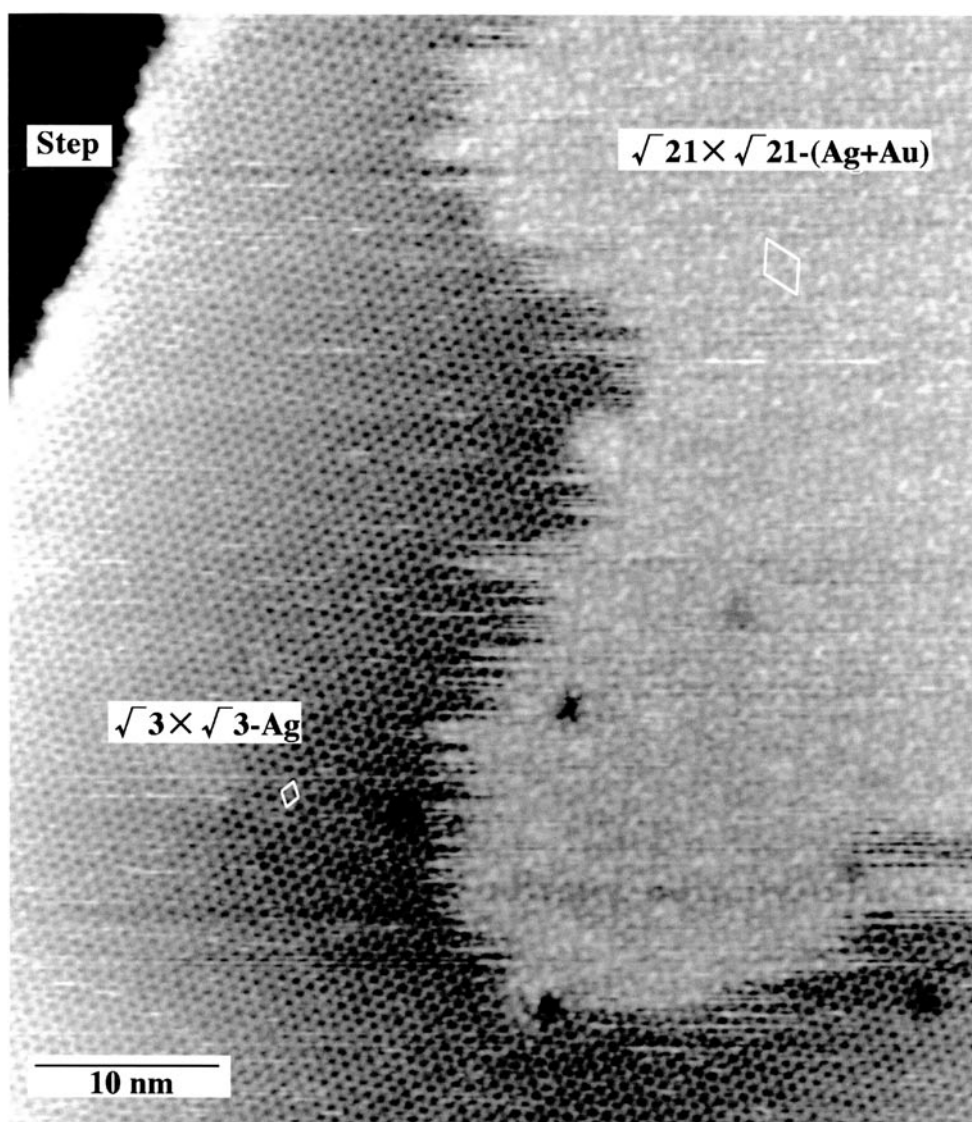
Figure 15. An STM image after Au deposition to about 0.1 ML coverage on top of the Si(111)–$\sqrt{3} \times \sqrt{3}$-Ag surface at RT, showing formation of the $\sqrt{21} \times \sqrt{21}$ domains. The unit cells of the $\sqrt{3} \times \sqrt{3}$ and $\sqrt{21} \times \sqrt{21}$ superstructures are shown by lozenges. The phase boundaries are very fuzzy because of mobile atoms. At about 0.2 ML coverage of Au, the surface is wholly covered with the $\sqrt{21} \times \sqrt{21}$ phase.

(figure 16(b)). All of these phases show high conductivities, as shown in figure 16. More than 0.2 ML coverage commonly destroys the $\sqrt{21} \times \sqrt{21}$ phases, resulting in reduction of the conductivity [71].

Similar phenomena—formation of a $\sqrt{21} \times \sqrt{21}$ superstructure and its enhanced conductivity—are found to occur also upon adsorptions of alkali metals on the $\sqrt{3} \times \sqrt{3}$-Ag surface at RT with coverages of around 0.2 ML, which is more than the critical coverages for the 2DAG phases [70].
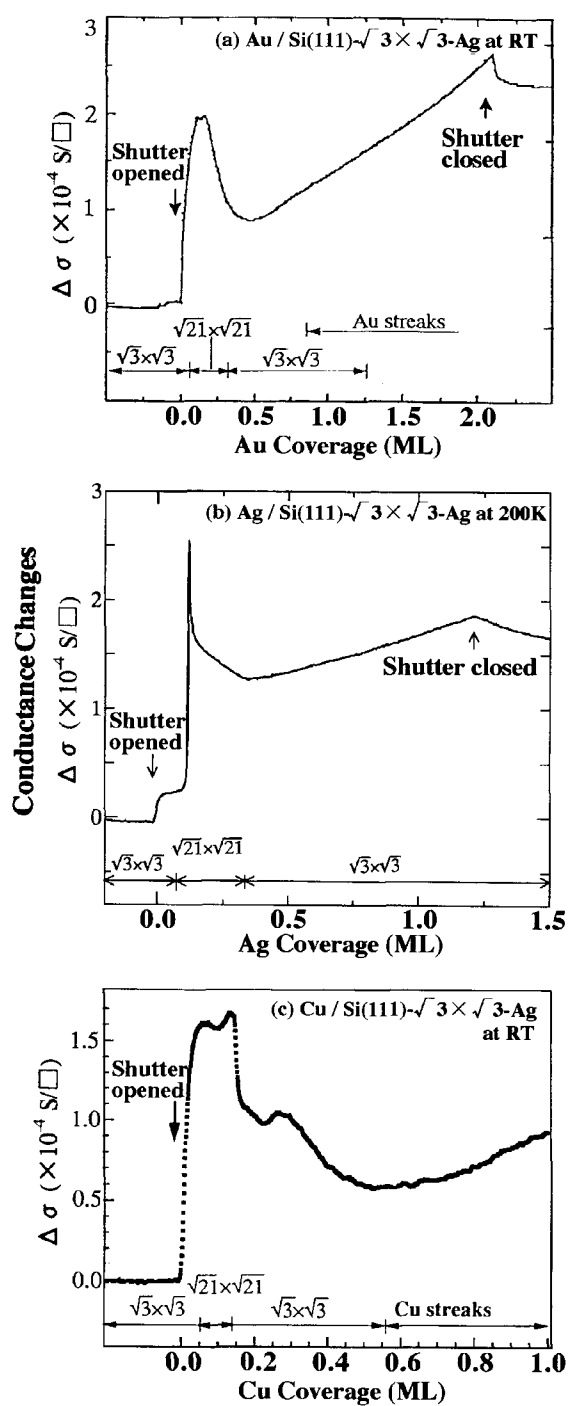
Figure 16. Changes in sheet conductance of a Si wafer during depositions of (a) Au, (b) Ag, and (c) Cu on the Si(111)–$\sqrt{3} \times \sqrt{3}$-Ag surface at ((a), (c)) RT and at (b) 200 K. The measurements were made continuously during the metal depositions. The surface structures indicated at the respective coverage ranges were confirmed by means of RHEED in separate runs of depositions under the same conditions.

In this way, monovalent adatoms at less than 0.1 ML coverage on the $\sqrt{3} \times \sqrt{3}$-Ag surface commonly adsorb as 2DAG phases, causing carrier doping into the surface-state band of the substrate and increasing the surface-state conductivity as described in the previous subsection, while at around 0.2 ML coverage they commonly form $\sqrt{21} \times \sqrt{21}$ superstructures, further increasing the conductivity [4].

The surface-state bands and band bending beneath the surface have already been investigated by photoemission spectroscopy for the $\sqrt{21} \times \sqrt{21}$ phases induced by noble-metal adatoms on the $\sqrt{3} \times \sqrt{3}$-Ag surface. As a result, the enhanced conductivities of the $\sqrt{21} \times \sqrt{21}$ phases are found to be not due to the surface-space-charge layers, but rather due to new metallic surface-state bands, indicated by S_1^* in figures 17(a) and 17(c), with large dispersions having larger Fermi wavevectors than the S_1 band of the initial $\sqrt{3} \times \sqrt{3}$-Ag surface (see figure 4(a)) [41, 71, 73].

In this way, it has been shown that the electrical conduction through surface-state bands can be experimentally detectable. But, its quantitative characterization under magnetic fields at various temperatures, and the influence of surface defects such as atomic steps and domain boundaries remain open questions to be addressed in future studies. Surface-state transport at the 1D metal surface, in the Si(111)–4 × 1-In superstructure introduced in section 4, is also quite interesting; this will be reported on elsewhere.

6. Microscopic four-point probes

By reducing the probe spacing in the four-point-probe method as shown in figure 11(b), one can expect a larger fraction of the current to flow near the surface, resulting in measurements that are more surface sensitive than those made using the macroscopic four-point probes (figure 11(a)) [74]. The actual current distribution in the crystal may not be as simple as expected from figure 11, because of a possible Schottky barrier between the surface states and the underlying bulk states [45] or a possible pn junction between the surface-space-charge layer and the interior bulk. But, the above simple expectation is more or less borne out, as demonstrated in our measurements. Miniaturization of the probes also enables avoidance of surface defects such as atomic steps, leading to an understanding of their influences on transport.

Figure 18 shows a SEM image of a microscopic four-point-probe chip, developed at Mikroelektronik Centret of the Technical University of Denmark [75, 76]†. Such probes with 4, 8, 10, 20, and 60 μm probe spacings were made using silicon-based microfabrication technology following a procedure similar to that used to fabricate microcantilevers for atomic-force microscopy. The probes are very flexible, which makes forming the contact to sample surfaces straightforward even when the sample plane is not aligned with the probes. The microscopic four-point probes were integrated in a UHV scanning electron microscope (SEM) with molecular beam epitaxy, enabling scanning RHEED and scanning reflection-electron microscopy (SREM) observations [77]. The microscopic four-point-probe chip was mounted on three sets of piezo-actuators for fine movements in X-, Y-, and Z-directions. The probes were made to approach the sample surface with the aid of *in situ* SEM observation, so we were able to make gentle contact with the selected area on the sample surface.

In order to obtain an almost step-free area that is as wide as possible on the Si(111) sample surface, we carried out repeated flash heatings by means of direct current up to 1200 °C for around one hour in total. After such treatment, the surface was separated into two regions, as shown in figure 19: step bunch regions around 2 μm wide and large flat terraces about 10 μm

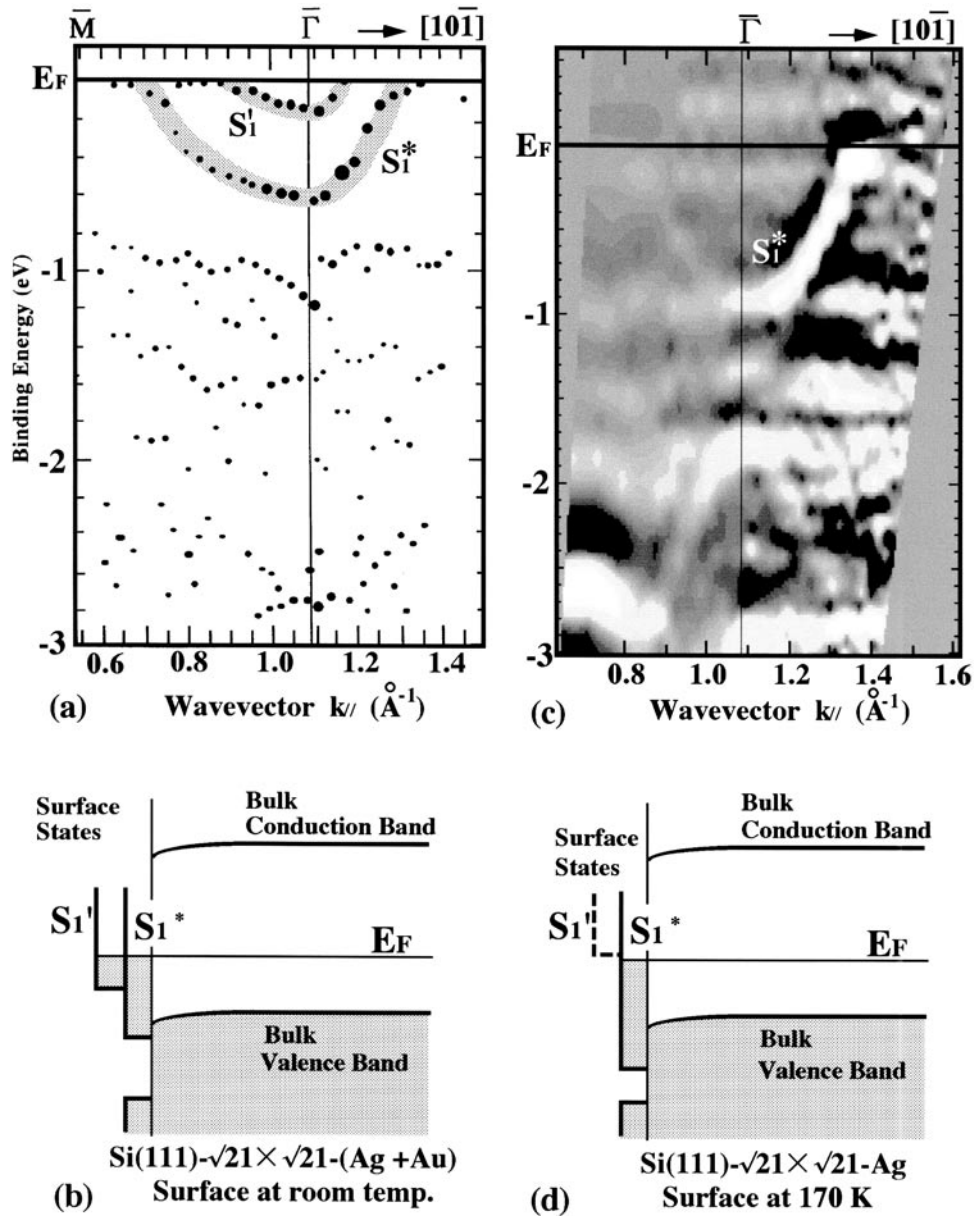† Microscopic four-point probes are now commercially available; http://www.capres.com.

Figure 17. Electronic structures of ((a), (b)) a Si(111)–$\sqrt{21} \times \sqrt{21}$-(Ag + Au) surface at RT and ((c), (d)) a Si(111)–$\sqrt{21} \times \sqrt{21}$-Ag surface at 170 K. (a) and (c) are 2D band dispersion diagrams constructed from ARPES measurements [41,73]. Although both of the S_1' and S_1^* states are observed in the Au-induced $\sqrt{21} \times \sqrt{21}$ phase, only the S_1^* state appears on the Ag-induced $\sqrt{21} \times \sqrt{21}$ surface; its S_1' band may be located above E_F. (b) and (d) are band diagrams representing the surface states and bulk states.

wide [78]. Thirty to fifty atomic steps are bunched in the step bunch regions, while only two or three monatomic steps run on the terrace regions. The monatomic steps are manifested as bright lines in figure 19(a) where small amounts of Ag deposition at 450 °C decorate step edges.
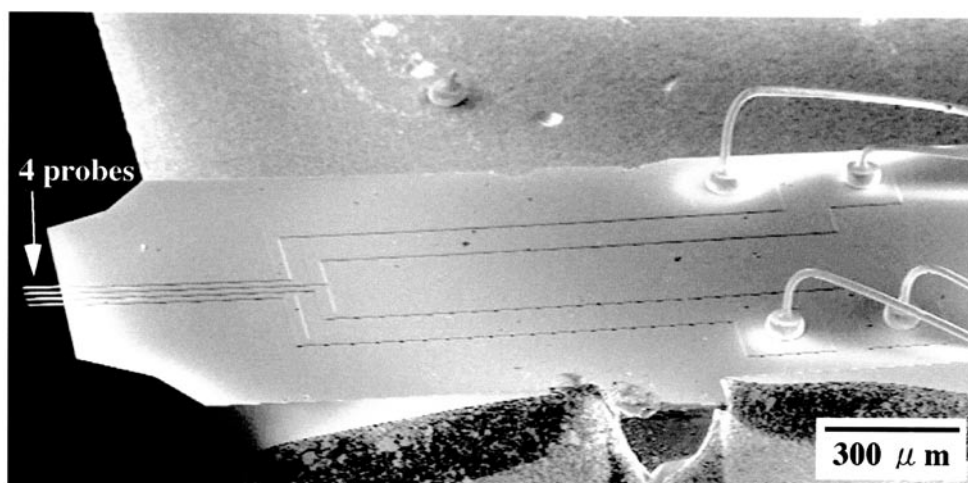
Figure 18. A SEM image of a microscopic four-point-probe chip [77].

The bright regions in figures 19(a), 19(b) are the Si(111)–$\sqrt{3} \times \sqrt{3}$-Ag superstructure domains, while the remaining dark areas are the Si(111)–7 × 7 clean domains. On increasing the Ag coverage up to one ML, the whole surface was covered by the $\sqrt{3} \times \sqrt{3}$-Ag superstructure as shown in figure 19(c); the surface structures were confirmed by *in situ* RHEED observations.

After preparing the large terraces having the 7 × 7 clean structure or $\sqrt{3} \times \sqrt{3}$-Ag structure, the microscopic four-point probes were brought into contact with the silicon surface, as seen in figure 20 where a probe chip with 8 μm spacing was used. The total probe width is larger than the width of the terrace, so the outer probes are positioned on neighbouring terraces. But, in figure 20(a), there is no step bunch running between the inner probes, measuring a voltage drop on an almost step-free terrace, while in figure 20(b), the inner probes measure a voltage drop across a step bunch. In this way, we can select the surface area under measurement by shifting the probes, so we can detect the influence of a step on the surface conductivity. In fact, we found that the resistance measured across a step bunch (figure 20(b)) was much larger than that measured on a terrace (figure 20(a)) for both the 7 × 7 and $\sqrt{3} \times \sqrt{3}$-Ag surfaces. This means directly that atomic steps on a surface cause an additional resistance, because of carrier scattering in the surface-state bands by step edges, as seen in the form of electron standing waves near step edges in the case of the $\sqrt{3} \times \sqrt{3}$-Ag surface (figure 5) [28], or because carriers in the surface-space-charge layer are diffusely scattered at step edges (due to surface roughness) in the case of the 7 × 7 surface [77, 79].

We also compared the resistances between the two surface structures measured on a terrace like that in figure 20(a). The resistance measured on the $\sqrt{3} \times \sqrt{3}$-Ag surface was smaller than that for the 7 × 7 clean surface by about two orders of magnitude [77, 79]. This should be compared with the result obtained using macroscopic four-point probes of about 10 mm probe spacing, described in section 5, where the difference in resistance between the two surfaces could be as small as about 15% [65]. These results mean that reducing the probe spacing makes the measurements more surface sensitive, as expected from figure 11. And also by reducing the step influence, the intrinsic difference between the two surfaces becomes revealed more dramatically.

By converting the measured resistances into sheet conductances, we confirmed that the extremely high conductance of the $\sqrt{3} \times \sqrt{3}$-Ag surface compared with that of the 7 × 7
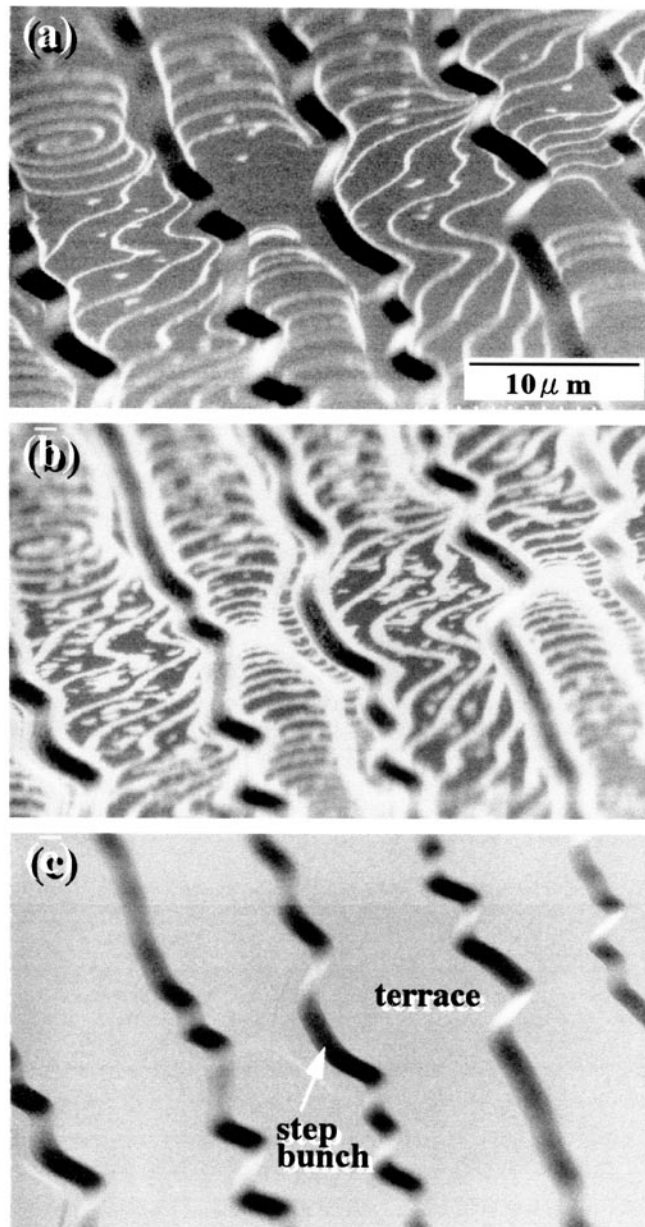
Figure 19. Grazing-incidence scanning electron micrographs of a step-bunched Si(111) surface. (a) and (b) show the partially Ag-covered surface, with the 7×7 (dark areas) and $\sqrt{3} \times \sqrt{3}$-Ag (bright areas) domains coexisting. The Ag coverages are around 0.1 and 0.4 ML, respectively. (c) shows the wholly Ag-covered $\sqrt{3} \times \sqrt{3}$-Ag surface, with 1 ML of Ag.

surface is attributable to the surface-state band inherent to the superstructure, rather than the conductivity of the surface-space-charge layer. Although this conclusion has already been reached on the basis of macroscopic four-point-probe measurements as described in section 5, microscopic four-point probes made it more convincing [79].
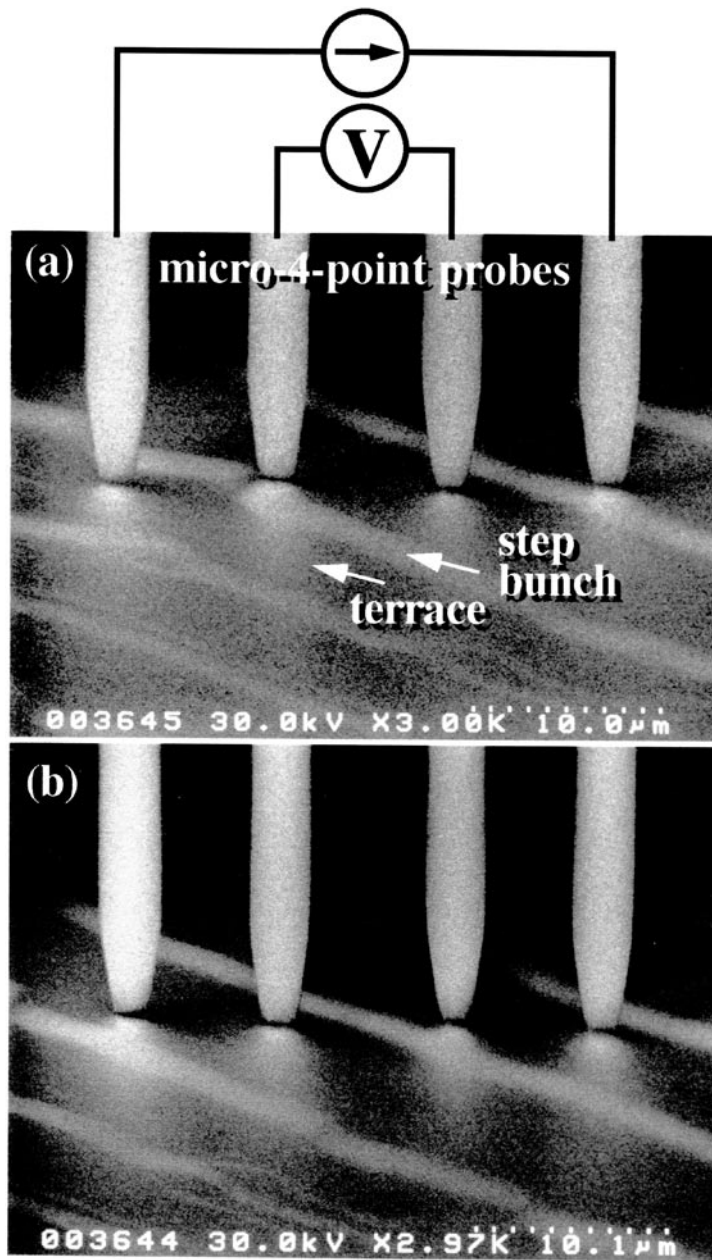
Figure 20. Scanning electron micrographs showing the microscopic four-point probes contacting with a silicon surface. The slightly brighter bands on the sample surface are step bunches, and the wider darker bands are terraces. The probes were shifted between (a) and (b) [77].

7. Conclusions

In the present review article, taking the silver- and indium-covered Si(111) surfaces as examples, various phenomena revealed in the surface-state bands are described. Some readers

may think that it is neither surprising nor new to find metallic electronic states and enhanced conductivity on silicon surfaces because metal atoms are deposited on them. But such considerations are too naive. The deposited metal atoms do not exhibit their own properties (those of their bulk crystals). The metal atoms do not make metallic bonds with each other to produce free electrons like in their bulks; rather, they make bonds with the substrate Si atoms to make characteristic surface electronic states. This is the feature of 'properties of surface phases', which are completely different from those of the bulk materials of the composite atoms.

Recently, electrical conduction through the dangling-bond state of the Si(111)–7×7 clean surface (state S_1 in figure 4(d)) was detected as characteristic changes in STM images [45]. The conductivity was found to be much lower than those of the $\sqrt{3} \times \sqrt{3}$-Ag and $\sqrt{21} \times \sqrt{21}$ surfaces by about four orders of magnitude. This gives a firm basis for our analyses of four-point-probe conductivity measurements in which the surface-state conductivity of the 7×7 clean surface was neglected. Although the dangling-bond-state band S_1 in figure 4(d) is known to be metallic (nearly half-filled), its dispersion is very small compared with that of the S_1 band of the $\sqrt{3} \times \sqrt{3}$-Ag surface of figure 4(a), which means a localized nature of the surface-state electrons, resulting in a very low conductivity. This may be seen to be reasonable by considering that this state comes from the dangling bonds of the topmost-layer Si atoms which are separated from each other by twice the 1×1 unit-cell edge of the bulk-terminated surface. Thus the atomic arrangements on the surface and the resulting electronic state directly characterize the conductivity. The 7×7 clean surface and the $\sqrt{3} \times \sqrt{3}$-Ag surface are quite instructive for comparison.

The electronic transport properties of surface-state bands will become increasingly important in the near future because of the necessity for semiconductor devices as well as the interest in the fundamental physics. With progress in miniaturization of microelectronic devices, the signal currents are forced to flow only near the surface regions of semiconductor crystals. Eventually the signal will be processed with current flow only through one or two atomic layers, where the surface electronic states play the main roles instead of the bulk states. Thus, studies of the transport properties of the surfaces presented here will lead to a branch of nanotechnology when coupled with fabrication technology for atomic-scale structures on surfaces.

Acknowledgments

References

[1] Lifshits V G, Saranin A A and Zotov A V 1994 *Surface Phases on Silicon* (Chichester: Wiley)
[2] Himpsel F J, Hollinger G and Pollak R A 1983 *Phys. Rev.* B **28** 7014
[3] Viernow J, Henzler M, O'Brien W L, Men F K, Leibsle F M, Petrovykh D Y, Lin J L and Himpsel F J 1998 *Phys. Rev.* B **57** 2321
[4] For a review, see Hasegawa S, Tong X, Takeda S, Sato N and Nagao T 1999 *Prog. Surf. Sci.* **60** 89
[5] For a review, see Hasegawa S, Jiang C-S, Nakajima Y, Nagao T and Tong X 1998 *Surf. Rev. Lett.* **3+4** 803
[6] Hasegawa S, Sato N, Shiraki I, Petersen C L, Bøggild P, Hansen T M, Nagao T and Grey F 2000 *Japan. J. Appl. Phys.* **39** 3815
[7] Takahashi T, Nakatani S, Okamoto N, Ishikawa T and Kikuta S 1988 *Japan. J. Appl. Phys.* **27** L753
   Takahashi T, Nakatani S, Okamoto N, Ishikawa T and Kikuta S 1991 *Surf. Sci.* **242** 54
   Takahashi T and Nakatani S 1993 *Surf. Sci.* **282** 17 and references therein
[8] Katayama M, Williams R S, Kato M, Nomura E and Aono M 1991 *Phys. Rev. Lett.* **66** 2762
[9] Watanabe S, Aono M and Tsukada M 1991 *Phys. Rev.* B **44** 8330
[10] Ding Y G, Chan C T and Ho K M 1991 *Phys. Rev. Lett.* **67** 1454
   Ding Y G, Chan C T and Ho K M 1992 *Phys. Rev. Lett.* **69** 2452
[11] LeLay G, Gothelid M, Cricenti A, Hakansson C and Perfetti P 1998 *Europhys. Lett.* **45** 65
[12] Yokoyama K, Ochi T, Sugawara Y and Morita S 1999 *Phys. Rev. Lett.* **83** 5023
[13] Sasaki N, Aizawa H and Tsukada M 2000 *Appl. Surf. Sci.* **157** 367
[14] Yamaguchi T 1999 *Meeting of the Physical Society of Japan (Hiroshima, March 1999)* vol 54, issue 1, part 2 (Tokyo: The Physical Society of Japan) abstracts, p 301
[15] Hong H, Aburano R D, Lin D S, Chen H and Chiang T-C 1992 *Phys. Rev. Lett.* **68** 507
   Hong H, Aburano R D, Lin D S, Chen H and Chiang T-C 1995 *Phys. Rev.* B **52** 1839
[16] Akimoto K, Lijadi M, Ito S and Ichimiya A 1998 *Surf. Rev. Lett.* **5** 719
[17] Weitering H H, Sullivan J P, Carolissen R J, Graham W R and Tung R T 1993 *Surf. Sci.* **70+71** 422
   Weitering H H, Sullivan J P and Carolissen R J 1993 *Appl. Surf. Sci.* **70+71** 422
   Weitering H H, Sullivan J P and Carolissen R J 1996 *J. Appl. Phys.* **79** 7820
[18] Komizo T, Hirayama H and Takayanagi K 1999 *Meeting of the Physical Society of Japan (Iwate, September 1999)* vol 54, issue 2, part 4 (Tokyo: The Physical Society of Japan) abstracts, p 831
[19] Kagami S, Minoda H and Yamamoto N 1999 *Meeting of the Physical Society of Japan (Kansai, March 1999)* vol 55, issue 1, part 4 (Tokyo: The Physical Society of Japan) abstracts, p 780
[20] Nagao T, Hildebrandt T, Henzler M and Hasegawa S 2000 *Phys. Rev. Lett.* submitted
[21] Aizawa H, Tsukada M, Sato N and Hasegawa S 1999 *Surf. Sci.* **429** L509
[22] Kondo Y, Nakamura J and Watanabe S 1999 *Int. Symp. on Surface Science for Micro- and Nano-Device Fabrication (Tokyo, November 1999)* (Tokyo: The Physical Society of Japan) abstracts, p 19
[23] Aizawa H and Tsukada M 1999 *Phys. Rev.* B **59** 10 923
[24] LeLay G, Gothelid M, Yu V Aristov, Cricenti A, Hakansson M C, Giammichele C, Perfetti P, Avila J and Asensio M C 1997 *Surf. Sci.* **377–379** 1061
[25] Nakayama T, Onoe J, Takeuchi K and Aono M 1999 *Phys. Rev.* B **59** 12 627
[26] Tsuchie K, Nagao T and Hasegawa S 1999 *Phys. Rev.* B **60** 11 131
[27] Iizumi K, Ueno K, Saiki K and Koma A 1999 *Meeting of the Physical Society of Japan (Iwate, September 1999)* vol 54, issue 2, part 4 (Tokyo: The Physical Society of Japan) abstracts, p 815
[28] Sato N, Nagao T and Hasegawa S 1999 *Phys. Rev.* B **60** 16 083
[29] Ichimiya A, Nomura H, Horio Y, Sato T, Sueyoshi T and Iwatsuki M 1994 *Surf. Rev. Lett.* **1** 1
[30] Nogami J, Wan K J and Lin X F 1994 *Surf. Sci.* **306** 81
[31] Homma I, Tanishiro Y and Yagi K 1991 *The Structure of Surfaces 3* ed S Y Tong, M A Van Hove, K Takayanagi and X D Xie (Berlin: Springer) p 610
[32] Zhang Z H, Hasegawa S and Ino S 1995 *Phys. Rev.* B **52** 10 760
[33] Jiang C-S, Tong X, Hasegawa S and Ino S 1997 *Surf. Sci.* **376** 69
[34] Tong X, Hasegawa S and Ino S 1997 *Phys. Rev.* B **55** 1310
[35] Tong X, Sugiura Y, Nagao T, Takami T, Takeda S, Ino S and Hasegawa S 1998 *Surf. Sci.* **408** 146

[36] Nagao T, S, Ohuchi, Matsuoka Y and Hasegawa S 1999 *Surf. Sci.* **419** 134
[37] Oura K, Lifshits V G, Saranin A A, Zotov A V and Katayama M 1999 *Surf. Sci. Rep.* **35** 1
[38] Sato N, Nagao T and Hasegawa S 1999 *Surf. Sci.* **442** 65
[39] Johansson L S O, Landemark E, Karlsson C J and Uhrberg R I G 1989 *Phys. Rev. Lett.* **63** 2092
Johansson L S O, Landemark E, Karlsson C J and Uhrberg R I G 1992 *Phys. Rev. Lett.* **69** 2451
[40] Hasegawa S, Tong X, Jiang C-S, Nakajima Y and Nagao T 1997 *Surf. Sci.* **386** 322
[41] Tong X, Jiang C-S and Hasegawa S 1998 *Phys. Rev.* B **57** 9015
[42] Sato N, Takeda S, Nagao T and Hasegawa S 1999 *Phys. Rev.* B **59** 2035
[43] Tersoff J and Hamann D R 1985 *Phys. Rev.* B **31** 805
[44] Avouris Ph, Lyo I-W and Walkup R E 1994 *J. Vac. Sci. Technol.* B **12** 1447
[45] Heike S, Watanabe S, Wada Y and Hashizume T 1998 *Phys. Rev. Lett.* **81** 890
[46] Li J, Schneider W-D, Berndt R and Crampin S 1998 *Phys. Rev. Lett.* **80** 3332
[47] Crommie M F, Lutz C P, Eigler D M and Heller E J 1995 *Surf. Rev. Lett.* **2** 127
[48] Yokoyama T, Okamoto M and Takayanagi K 1998 *Phys. Rev. Lett.* **81** 3423
[49] Yokoyama T and Takayanagi K 1999 *Phys. Rev.* B **59** 12 232
[50] Nakajima Y, Takeda S, Nagao T, Hasegawa S and Tong X 1997 *Phys. Rev.* B **56** 6782
[51] Saranin A A, Lifshits V G, Katayama M and Oura K 2000 *Japan. J. Appl. Phys.* **39** L306
[52] Bunk O, Falkenberg G, Zeysing J H, Lottermoser L, Johnson R L, Nielsen M, Berg-Rasmussen F, Baker J and
Feidenhans'l R 1999 *Phys. Rev.* B **59** 12 228
[53] Abukawa T, Sasaki M, Hisamatsu F, Goto T, Kinoshita T, Kakizaki A and Kono S 1995 *Surf. Sci.* **325** 33
[54] Hill I G and McLean A B 1997 *Phys. Rev.* B **56** 15 725
[55] Yeom H W, Takeda S, Rotenberg E, Matsuda I, Horikoshi K, Schaefer J, Lee C M, Kevan S D, Ohta T, Nagao T
and Hasegawa S 1999 *Phys. Rev. Lett.* **82** 4898
[56] Kumpf C, Bunk O, Zeysing J H, Su Y, Nielsen M, Johnson R L and Feidenhans'l R 2000 *Phys. Rev. Lett.*
submitted
[57] Nishiguchi T, Kageshima M, Ara-Kato N and Kawazu A 1998 *Phys. Rev. Lett.* **81** 3187
[58] Ishida M, Mori T and Shigekawa H 1999 *Phys. Rev. Lett.* **83** 596
[59] Grüner G 1994 *Density Waves in Solids* (Reading, MA: Addison-Wesley)
[60] LeLay G, Hasegawa S, Aristov V Yu, Giovanelli L, Takeda S, Enriquez H, Derycke V, Soukiassian P, Belkhou R
and Taleb-Ibrahimi A 2000 to be published
[61] Henzler M 1975 *Surface Physics of Materials I* ed J M Blakely (New York: Academic) p 241
[62] Hasegawa S and Ino S 1992 *Phys. Rev. Lett.* **68** 1192
[63] Kono S, Higashiyama K, Kinoshita T, Miyahara T, Kato H, Ohsawa H, Enta Y, Maeda F and Yaegashi Y 1987
Phys. Rev. Lett. **58** 1555
[64] Sze S M 1981 *Physics of Semiconductor Devices* 2nd edn (New York: Wiley)
[65] Jiang C-S, Hasegawa S and Ino S 1996 *Phys. Rev.* B **54** 10 389
[66] Nakajima Y, Uchida G, Nagao T and Hasegawa S 1996 *Phys. Rev.* B **54** 14 134
[67] Cusack N E 1987 *The Physics of Structurally Disordered Matter* (Bristol: Hilger)
[68] Yasunaga H and Natori A 1992 *Surf. Sci. Rep.* **15** 205
[69] Natori A, Murayama M and Yasunaga H 1996 *Surf. Sci.* **357+358** 47
[70] Hasegawa S, Tsuchie K, Toriyama K, Tong X and Nagao T 2000 *Appl. Surf. Sci.* **162+163** 42
[71] Tong X, Jiang C-S, Horikoshi K and Hasegawa S 2000 *Surf. Sci.* **449** 125
[72] Hasegawa S and Ino S 1993 *Int. J. Mod. Phys.* B **7** 3817
[73] Tong X, Ohuchi S, Tanigawa T, Matsuda I, Nagao T and Hasegawa S 2000 *Phys. Rev.* B to be submitted
[74] Hasegawa S 2000 *Curr. Opin. Solid State Mater. Sci.* at press
[75] Bøggild P, Petersen C L, Grey F, Hassenkam T, Björnholm T, Shiraki I and Hasegawa S 1999 *Proc. Transducer
99 (Sendai, June 1999)*
[76] Petersen C L 1999 Microscopic four-point probes *PhD Thesis* Mikroelektronik Centret, DTU Building 345 East,
DK-2800 Lyngby, Denmark
[77] Shiraki I, Petersen C L, Bøggild P, Hansen T M, Nagao T, Grey F and Hasegawa S 2000 *Surf. Rev. Lett.* at press
[78] Latyshev A V, Krasilnikov A B and Aseev A L 1994 *Surf. Sci.* **311** 395
[79] Shiraki I, Petersen C L, Bøggild P, Hansen T M, Nagao T, Grey F and Hasegawa S 2000 *Nature* submitted